AIAA SciTech
4-8 January 2016, San Diego, California, USA
34th Wind Energy Symposium

Interaction of Atmospheric Turbulence with Blade Boundary Layer Dynamics on a 5MW Wind Turbine using Blade-Boundary-Layer-Resolved CFD with hybrid URANS-LES

Ganesh Vijayakumar* James G. Brasseur† Adam Lavely‡ Balaji Jayaraman§
Brent. C. Craven¶
Pennsylvania State University, University Park, PA

Modern commercial megawatt-scale wind turbines occupy the lower 15-20% of the atmospheric boundary layer (ABL), the atmospheric surface layer (ASL). The current trend of increasing wind turbine diameter and hub height increases the interaction of the wind turbines with the upper ASL which contains spatio-temporal velocity variations over a wide range of length and time scales. This work centers on the development of a computational framework to simulate the interaction between the atmospheric and wind turbine blade turbulence dynamical systems using a two step one-way coupled approach. Pseudo-spectral large eddy simulation (LES) is used to generate a true (equilibrium) atmospheric boundary layer over a flat land with specified surface roughness and heating consistent with the stability state of the daytime lower troposphere. Using the data from the precursor simulation as inflow conditions, a second simulation is performed on a smaller domain around the wind turbine using finite volume CFD with a body-fitted grid to compute the unsteady blade loads in response to atmospheric turbulence. The ability of our computational framework to capture blade boundary layer dynamics in response to atmospheric turbulence is intimately associated with the design of our grid and with the development of a new hybrid URANS-LES turbulence model. The new turbulence model blends a 1-equation LES subgrid model in the far field with the $k-\omega-SST-SAS$ URANS model to the blade boundary layer adjacent to the blade surface. With this computational framework, we simulated a single rotating blade of the NREL 5MW wind turbine in the moderately convective daytime atmosphere using blade-boundary-layer-resolved CFD simulations.

The analysis of load fluctuations on a single rotating blade in a daytime atmosphere using blade-boundary-layer-resolved CFD has yielded two key results: (1) Whereas non-steady blade loadings are generally described as the response to non-steadiness in wind *speed*, our analysis show that time changes in wind vector *direction* are a much greater contributor to load transients, and strongly impact boundary layer dynamics; (2) largest temporal variations in loadings result from three distinct dynamical responses with disparate time scales: advection of atmospheric eddies through the rotor at the minute time scale, blade response at the rotor rotation time scale ($\sim 5s$) and blade response to turbulence-induced forcings as the blades traverse internal atmospheric eddy structure at sub-blade rotation time scales. In our simulations at rated wind speed, quasi-2D blade boundary layer separation is observed over most of the outer 50% of the blade with chordwise motions, correlated with time changes in relative wind vector angle, which itself is strongly correlated with changes in blade sectional and integrated loads. Thus, tools based on sectional "table lookups" like FAST[1] and Actuator Line Methods,[2] improved using data from high-fidelity simulations and experiment, have the potential to capture the major fluctuations in integrated loads from daytime atmospheric turbulence.

*Graduate Student, Department of Mechanical Engineering, AIAA Student Member.
†Professor, Department of Mechanical Engineering, AIAA Member.
‡Graduate Student, Department of Aerospace Engineering, AIAA Student Member.
§Research Associate, Department of Mechanical Engineering, AIAA Member.
¶Head of the Computational Methods Development Department, Applied Research Laboratory.

I. Introduction

Wind turbines have been consistently increasing in size over the last decade.[3] Modern commercial wind turbines operate in the lower 15-20% of the Atmospheric Boundary Layer (ABL), also known as the Atmospheric Surface Layer (ASL). The ABL contains strong coherent turbulent motions[4] that interact with wind turbines. Though the ABL is also a turbulent high Reynolds number boundary layer, it differs from the canonical shear-driven flat plate boundary layer due to new aspects such as the interaction of buoyancy and surface heating, Coriolis force, and the existence of a capping inversion. While the current IEC design standard for wind turbines[5] characterizes atmospheric turbulence through turbulence intensity and velocity spectra alone, more recent efforts like those by Wharton and Lundquist[6] have focused on measuring the effect of the stability state of the atmosphere on the shear profiles across the rotor disk, Monin-Obukhov length and cross-correlations of velocity components. Table 1 shows the wide range of length and time scales of motions in an Atmospheric Boundary Layer.

	Time Scale	Length Scale	Modeling Technique
Wind Turbine	$\approx \mathcal{O}$(revolution period, seconds)	$\approx \mathcal{O}$(1-100m) Blade chord - rotor diameter	CFD, actuator methods, BEMT
Energy containing ABL turbulence structure	$\approx \mathcal{O}$(seconds-minutes) depending on ABL stability state	$\approx \mathcal{O}$(10-100m) depending on distance from surface	LES of equilibrium ABL at prescribed stability state
Mesoscale modulations	$\approx \mathcal{O}$(hours-days)	$\approx \mathcal{O}$(tens-hundreds km)	Prescribed geostrophic wind and surface heating

Table 1: Length and time scales in ABL relevant to wind turbine aerodynamics.

The main objective of this work is to determine the first order mechanisms of the interaction of day-time atmospheric turbulence with aerodynamics of commercial MW scale wind turbines across all relevant length and time scales. There are two main tools required to achieve this objective, the first is a tool to get realistic inflow conditions for a wind turbine in the atmosphere and the second is a tool to compute the loads on the wind turbine.

To obtain inflow conditions for a wind turbine in the field, synthetic turbulence generators have been designed[7,8,9,10] based on measured spectra and velocity variances. Another approach used to obtain inflow conditions is Large Eddy Simulation (LES) of the ABL. Several studies[11,12,13] have compared the loads on the wind turbine using inflow generated from synthetic turbulence generators and using LES of ABL. Synthetic turbulence generators fail to generate the streamwise and vertical coherence of the turbulence structures and hence are unable to reproduce the variance in the loads. LES of ABL, albeit computationally expensive compared to synthetic turbulence generators, is an existing method that is capable of generating turbulence in the ASL with the right spectra, variance profiles and streamwise and vertical coherence in the resolved (large) scales. We use LES of ABL to simulate a realistic day-time atmosphere for this work.

The second tool required for this work is a method to compute the aerodynamic loads on the wind turbine. All models other than full CFD of wind turbines use some form of the Blade Element Momentum (BEM) theory;[14,15,16] they only differ in the method with which the upwash is calculated at each blade station and is indirectly related to the assumptions of the wake structure in the model. 3D flow effects on a turbine blade are expected to be high when a wind turbine is operating in real atmospheric turbulence compared to uniform inflow. The changes in the angle of attack on the blade due to turbulence structures in the Atmospheric Surface Layer are large compared to the mean Angle of Attack (AoA).[17] These changes in the AoA can cause the airfoil to stall (flow separation) and cause significant unsteady 3D flow and the resultant fluctuations on the blade loadings. The current state of the art tools to model unsteady aerodynamics on wind turbine blades using BEM theory based methods are incapable of resolving these flow structures to the accuracy desired in the current work.[18] Hence, we have developed and used a computational environment using blade boundary layer resolved CFD of the flow around the wind turbine to obtain the aerodynamic loads.

Thus, we use a two step one-way coupled approach to simulate the interaction between the atmospheric and wind turbine blade turbulence dynamical systems. This work is performed as a part of the blade

aerodynamics and ABL module of the Penn State Cyber Wind Facility (CWF). The CWF centers on the creation of a CFD framework to realistically simulate a wind turbine in the field at the highest possible levels of resolution and fidelity within current HPC environments. The first key element of the CWF is the accurate representation of atmospheric turbulence with high fidelity LES in the numerical prediction of aerodynamic loadings on wind turbine blades. This component is missing or modeled kinematically in all other high fidelity CFD studies of wind turbine aerodynamics. Pseudo-spectral large eddy simulation (LES) is used to generate a true (equilibrium) atmospheric boundary layer over a flat land with specified surface roughness and heating consistent with the stability state of the daytime lower troposphere. Using the data from the precursor simulation as inflow conditions, a second simulation is performed on a smaller domain around the wind turbine using finite volume CFD with a body-fitted grid to compute the unsteady blade loads in response to atmospheric turbulence. Thus another key element of the CWF is the capture of near-blade-surface boundary layer dynamics at the highest possible accuracy using hybrid URANS-LES. To reduce the complexity of the simulation, we focus on simulating the flow around a rigid Single Rotating Blade of the NREL 5MW turbine[1] in the Atmosphere (SRBIA) operating in Region III with constant rpm and fixed pitch.

Section II describes the computational algorithm and environment of the Cyber Wind Facility simulation of the NREL 5MW turbine blade along with a brief review of the existing literature on the state of the art methods for each component. The advances in the understanding of ABL - Wind turbine interaction obtained from this work are described in Section III. These advances are summarized in section IV along with a few conclusions.

II. Computational Algorithm and Environment of CWF simulations

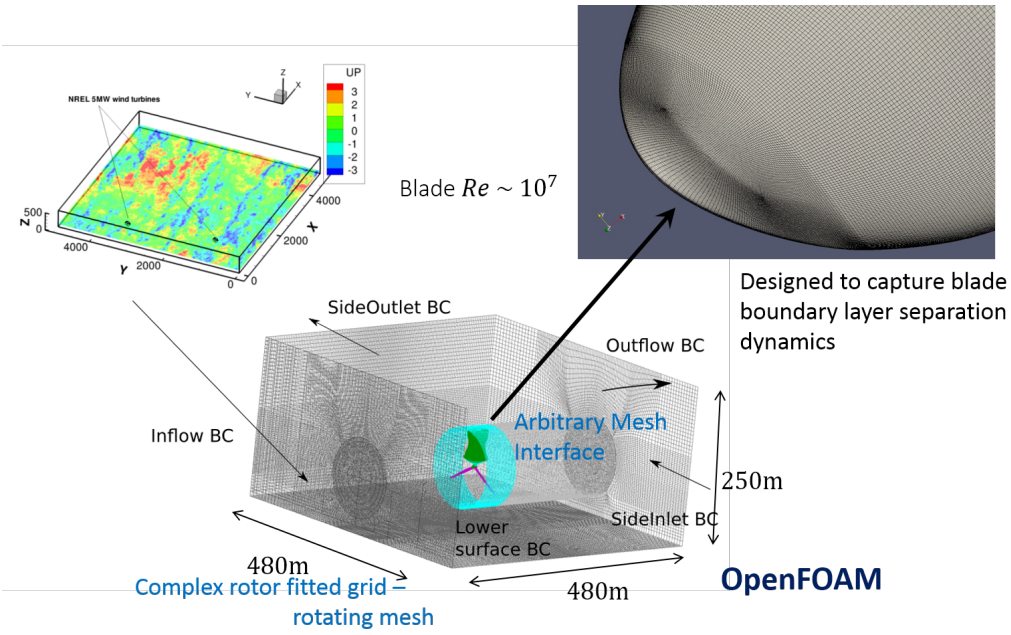

Figure 1: Illustration of coupling the LES of ABL with CFD of flow around the wind turbine.

Figure 1 shows the two-step one way coupled approach to simulate the interaction of ABL turbulence with wind turbine aerodynamics. This approach resolves all the relevant length and time scales from the integral scales of the ABL to the blade boundary layer separation dynamics length scales. Section II.A describes the precursor LES of ABL to obtain inflow conditions for the turbine. Using these inflow conditions a second simulation is performed using a complex rotor fited grid and a partly rotating mesh to compute the flow around the entire NREL 5MW turbine blade along with the effect of the ground. The domain for the second simulation is $4D \times 4D \times 2D$, where D is the diameter of the turbine. The details of the solver, grid and domain for this simulation are described in Sections II.B and II.C. Section II.D describes the new

Hybrid URANS-LES model developed to capture the energy containing eddies in the ABL along with the blade boundary layer separation dynamics. Finally, Section II.E describes the process of obtaining initial conditions for the *SRBIA* simulation.

II.A. LES of ABL to Generate a Realistic Flow Field in a Daytime Atmosphere

Sullivan and Patton[19] have developed a highly parallel implementation of the algorithm in[20] that scales up to 16000 processors; this code was used to carry out LES of ABL with the resolution of the order of the blade chord ($\sim 3m$) in the vicinity of the wind turbine. The high resolution also allows the simulation to be closer to the "High Accuracy Zone" (HAZ) as defined by Brasseur and Wei[21] to capture Law of the Wall. The parameters for this simulation are given in Table 2.

Domain	Grid	Smagorinsky constant	Surface Temperature Flux	Geostrophic wind
$5.12 \times 5.12 \times 2.048$ km	$512 \times 512 \times 256$	0.08	$0.2Km/s$	$15m/s$

Table 2: Details of the Moderately Convective Boundary Layer precursor simulation performed using the algorithm of Sullivan and Patton.[19]

Inflow Conditions for Wind Turbine CFD

Once the simulation reaches a quasi-stationary state, data is extracted at every time step ($\sim 0.5s$) for about 30 minutes ($\sim 2-3$ eddy turnover times). The three velocity components, temperature and sub-filter scale kinetic energy are stored over the entire horizontal domain at all grid levels upto $250m$ in height. This data is stored to allow the placement of a wind turbine at any location and direction. Appropriate planes are then extracted from this data set and used as inlet boundary conditions in the wind turbine CFD domain.

II.B. Design of Solver to Simulate the Flow Around a Wind Turbine in an ABL

Navier-Stokes computations of loads on full scale wind turbines started due to the availability of rotor geometry and validation data through the NREL-VI experiments.[22] Most computations were restricted to solving the Reynolds-Averaged Navier-Stokes equations in a rotating frame of reference attached to a blade using periodic boundary conditions in the azimuthal direction using structured multiblock or overset grids, a model for the Reynolds stresses (Le Pape and Lecanu,[23] Sørensen et al.,[24] Lynch and Smith[25] - $k-\omega-SST$, Potsdam and Mavripilis[26] - Spalart-Allmaras, Duque et al.[27] - Baldwin-Barth, Johansen et al.[28]) and the NREL-VI rotor geometry. All of the above studies used uniform inflow conditions with specified turbulence intensity. More recent efforts have focused on full NS computations of MW scale wind turbines (Sørensen et al.,[29] Bazilevs et al.,[30,31] Chow and van Dam,[32,33] Zahle et al.[34]). The existing literature points to the success of full Navier-Stokes computations in predicting wind turbine loads under attached flow conditions and indicate a need for using hybrid URANS-LES methods to capture stalled flow regimes accurately.

There have been no computations of flow around wind turbines under realistic atmospheric inflow conditions, a capability that is central to our CWF developments and our research objectives. To develop this capability, Vijayakumar et. al.[35] extended the pseudo-spectral LES of ABL algorithm and the corresponding boundary conditions to the finite volume method using the OpenFOAM[36] libraries. They demonstrated the capability of the solver to accurately propagate the ABL turbulence structures, provided through inflow conditions from a precursor pseudo-spectral LES, through a finite volume domain without dissipation. The solver for the current *SRBIA* simulations is developed by combining solver of Vijayakumar et. al.[35] with that for a moving mesh. The mesh inside the cylindrical region in cyan in Figure 1 is rotating with respect to the outer fixed mesh. The flux relative to the moving mesh is used to solve the Navier-Stokes regions in the rotating regions.

II.C. Design of Domain and Grid to Perform the Simulation

The flow around a wind turbine in an atmospheric boundary layer has been shown to encompass a wide range of length scales in Tables 3 and 1. While the integral scales of the atmospheric boundary layer are

$\sim O(10-100m)$ in the horizontal, the viscous surface layer of the blade boundary layer is $\sim O(10-100\mu m)$. This separation in scales requires a grid design for *SRBIA* that resolves the appropriate scales at every location while providing a sufficiently smooth transition in the grid to both maintain numerical stability and allow the turbulence to full the spectrum to the smallest resolved scales. The domain of the simulation is designed to be $\sim O($ multiple rotor diameters). At the inlet of the domain, the grid is designed to be similar to the grid of the high-resolution precursor ABL simulation described in Table 2. The grid is gradually refined up to $\sim 2-3$ chord lengths surrounding the turbine blade, where it interfaces with the extruded structured grid from the blade surface. The details of the CAD model of the NREL 5MW turbine blade developed for this purpose are described in Vijayakumar et. al.[37] The grid near the blade surface is designed to accurately model the blade boundary layer with $y^+ \sim O(1)$ at the first grid cell adjacent to the surface. The analysis of wind turbine response to atmospheric turbulence using BEM theory by Lavely et. al.[17] pointed to the importance of *Local Flow Angle* on load fluctuations. The atmospheric boundary layer causes large fluctuations in the flow angle near the middle sections of the blade that could potentially cause transient boundary layer separation. We hypothesized that spanwise motion of the boundary layer separation might contribute to temporal torque fluctuations. For this reason, parked blade simulations at high angle of attack were carried out to estimate grid resolution requirements. The blade surface mesh was resolved with over 700 points in the spanwise direction in an attempt to capture potential spanwise fluctuations.

The cyan region in Figure 1 is rotated with respect to the outer mesh using a sliding approach implemented using the Arbitrary Mesh Interface (AMI) in OpenFOAM.[36] The grid is designed to resolve the appropriate length scales in different parts of the domain. The grid resolution near the inlet of the domain is designed to very similar to the precursor simulation of the ABL, while the resolution near the blade is designed to capture the blade boundary layer separation dynamics. The wall normal resolution near the blade is designed to capture the viscous surface layer with $y^+ \approx 1$. The viscous surface layer is designed using high aspect ratio cells as the turbulence model operates in the URANS mode. As the grid is extruded from the blade surface, it is designed to achieve an aspect ratio of 1 where the LES mode is triggered in the hybrid URANS-LES model.

II.D. Hybrid URANS/LES Turbulence Model Across a Disparate Range of Length Scales

The interaction of a wind turbine with atmospheric turbulence spans a very wide range of length and time scales as shown in tables 1 and 3. The boundary layer on the rotor blade does not experience the atmospheric turbulence as turbulence but instead as a time varying mean flow. The length scales of the flow features near the blade (boundary layer dynamics, separation, vortex shedding, etc.) are orders of magnitude smaller than the energy-containing eddies in atmospheric turbulence. No single turbulence model is known to work over such a wide range of length and time scales. The interaction between eddies of such disparate length scales is part of our research. None of the current hybrid URANS-LES methods or SAS capture this interaction.

	Time Scale	Length Scale	Turbulence modeling strategy
Dominant Energy containing motions in ASL	$\sim \mathcal{O}$(minutes) multiple turbine rotation time scales	$\sim \mathcal{O}$(10-1000m)	LES - 1 eq model
Tip vortex, other shed vortex, separation on blade	$\sim \mathcal{O}(c/u_{rel})$	$\sim \mathcal{O}$(blade chord)	SAS (RANS like to LES like)
Attached boundary layer on turbine blade	$\sim \mathcal{O}(\delta/u_{rel})$	$\sim \mathcal{O}(\delta)$	$k-\omega-SST$ RANS

Table 3: Length and time scales of flow in different regions of a wind turbine.

Large eddy simulation should resolve the energy containing scales of turbulence and model the effects of the unresolved scales on the resolved scales. In application, most "sub-filter" (SFS) stress and flux models only treat the loss of turbulent kinetic energy from resolved to SFS scales. The integral scales are known to reduce with distance from the wall in high Reynolds number boundary layers. Resolving the surface

viscous layers or roughness elements with LES is impossible or impractical at the high Reynolds numbers of commercial wind turbine and atmospheric flows,[38,39] Piomelli and Balaras[40] review the "wall models" in LES to bypass the wall layer resolution requirement; these models directly specify the effect of the surface on the flow through an effective shear stress. Wall-modeled LES requires some prior knowledge of the flow or homogeneity in the geometry. Spalart et al.[41] proposed the first hybrid URANS-LES method for arbitrary external aerodynamics applications using the Spalart-Allmaras turbulence model,[42] now known as "Detached Eddy Simulation". Travin et al.[43] extended the DES formulation to the $k-\omega-SST$ model. Sorensen et al.,[44] Johansen et al.,[28] Stone et al.[45] and Lynch and Smith[25] have used this model to predict the unsteady separation on wind turbine blades of full scale rotors.[46,47] provide other reviews of the DES methodology.

The transition from RANS to LES in hybrid URANS-LES is dependent on the grid in relationship to turbulence scales. The development of LES turbulence after separation has been found to be very sensitive to the grid.[39] Improvements to basic DES have focused on using flow features in addition to the grid to improve this transition.[48,49,50,51,52] Menter and Egorov[53,54,55,56] took this concept further and proposed a Scale Adaptive Simulation model within the RANS framework. The model relies on the "instability" in the flow, measured by the ratio of the first gradient to the second gradient in the velocity, to transition the simulation from being "RANS like" to "LES like."

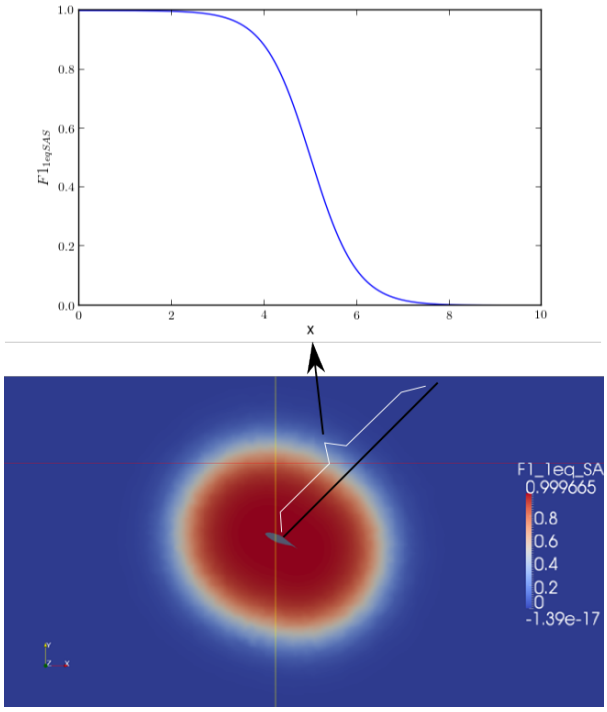

(a): The tanh function used to blend the URANS and LES regions.

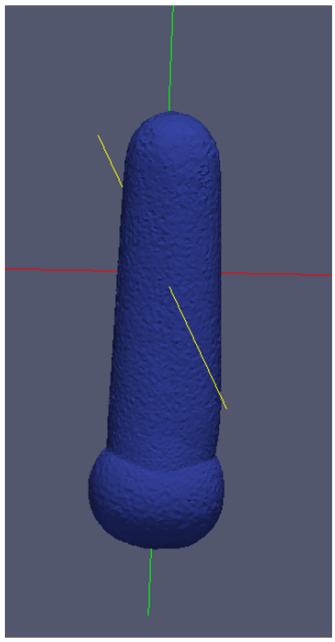

(b): Isosurface of $F1_{1eqSAS} = 0.5$ around one blade.

Figure 2: Illustration of the blending function between the $k-\omega-SST-SAS$ model near the blade and the 1 equation LES model away from the blade.

The objective of this work is to use the turbulence model that is known to work best at each scale and blend them together smoothly into a unified framework. Hence, the blade boundary layer region is modeled using the $k-\omega-SST$ RANS model, one of the best available today to predict separation for external aerodynamics applications. The SAS model[55] is used to allow the simulation to transform from a RANS model in the attached boundary layer to an LES like simulation in the separated regions of the blade. The ABL turbulence is modeled using the one equation model in Moeng.[20] An explicit blending function $F1_{1eqSAS}$ is used to blend the SAS model near the blade with the one equation LES model away from the blade. The blending function is based on the distance from the blade wall. The current choice for this function is a tanh function shown in Figure 2. The details of the turbulence model are described in Vijayakumar et. al.[37] The new blended turbulence model allows us to use the best available turbulence

model in each of the regions described in table 3. The OpenFOAM[36] framework allowed the implementation of the blended turbulence model with relative ease. This turbulence model is used to perform the highly resolved computations of the flow around the turbine.

II.E. Development of initial conditions for the *SRBIA* simulation

To develop the initial conditions for the final simulation, the flow around an NREL 5MW blade is first simulated in a cylindrical domain with uniform inflow of 14m/s. The Navier-Stokes equations are solved in a rotating frame of reference by adding terms corresponding to Coriolis and Centrifugal forces. The flow field from this simulation near the blade is blended with the one from the precursor ABL away from the blade to create the initial condition for the *SRBIA* simulations.

III. Results

This section describes the advances in the understanding of ABL - Wind turbine interaction mechanisms obtained using the two-step one way coupled approach described in the previous sections. Section III.A motivates the results to come by analyzing the characteristics of daytime atmospheric turbulence relevant to unsteady wind turbine response. Using these results, Section III.B describes the motivation for the choice of the initial location of the wind turbine. The response of the integrated loads of the Single Rotating Blade in the Atmosphere computed using CFD is described in Section III.C. Subsequent sections then split the integrated moments into sectional loads and describe the mechanism of load fluctuations in each section and their contribution to the integrated load fluctuations.

III.A. Characteristics of Daytime Atmospheric Turbulence Relevant to Unsteady Wind Turbine Response

The ABL contains fluctuations in the velocity at many different length and time scales. However, the objective here is to quantify the scales that are relevant to the unsteady loads on commercial, megawatt scale turbines. As a first step, an ABL flow field generated using LES is sampled to extract the relevant scales. The sampling is performed on a "hypothetical" NREL 5MW turbine to match the dimensions of the turbine and it's relation to the turbulence structure of the ABL. Thus, the "hypothetical" wind turbine analysis does not use a real turbine; instead, it uses the dimensions and the operational characteristics (for e.g. rpm) of a realistic turbine to sample the ABL. As rotating turbine blades cut through atmospheric eddies passing through the rotor disk, fluctuations in sectional and integrated loads occur at a range of time scales. The outer 60-95% of a turbine blade is known to contribute most of the integrated moments around the blade root. Hence the forcing experienced by a point at 75% span, near maximum sectional lift, is representative of the forcing on the turbine blade.

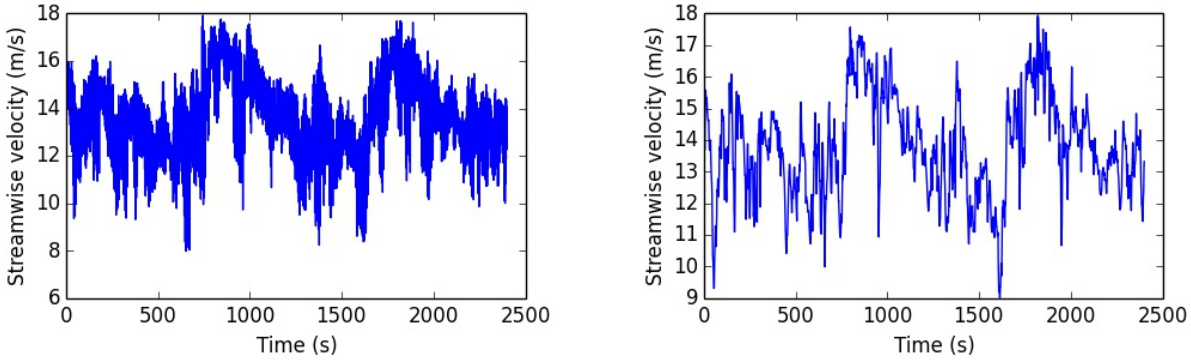

(a): 75% span (b): Hub

Figure 3: Streamwise velocity measured at two different points on a hypothetical NREL 5MW turbine in an ABL.

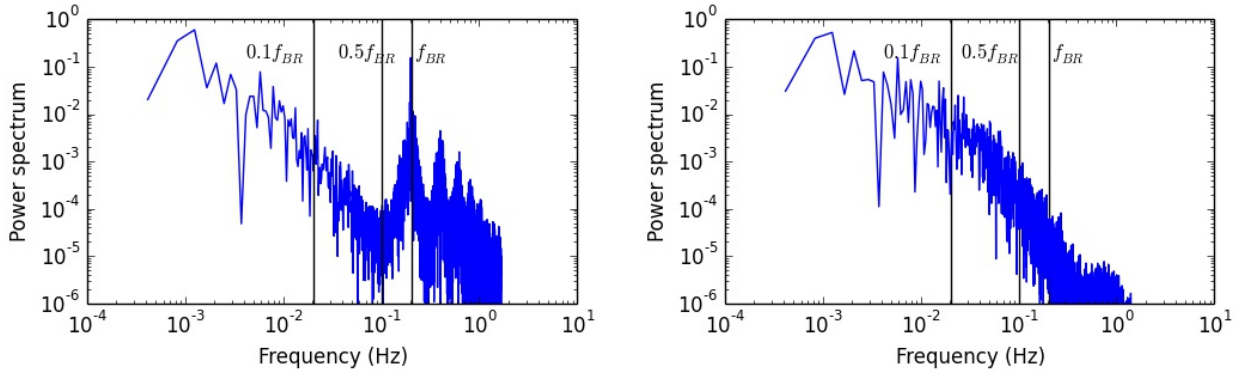

(a): 75% span (b): Hub

Figure 4: Power spectrum of the streamwise velocity measured at two different points on a hypothetical NREL 5MW turbine in an ABL. The three black lines are at $0.1f_{BR}$, $0.5f_{BR}$ and f_{BR} where f_{BR} is the blade rotation frequency.

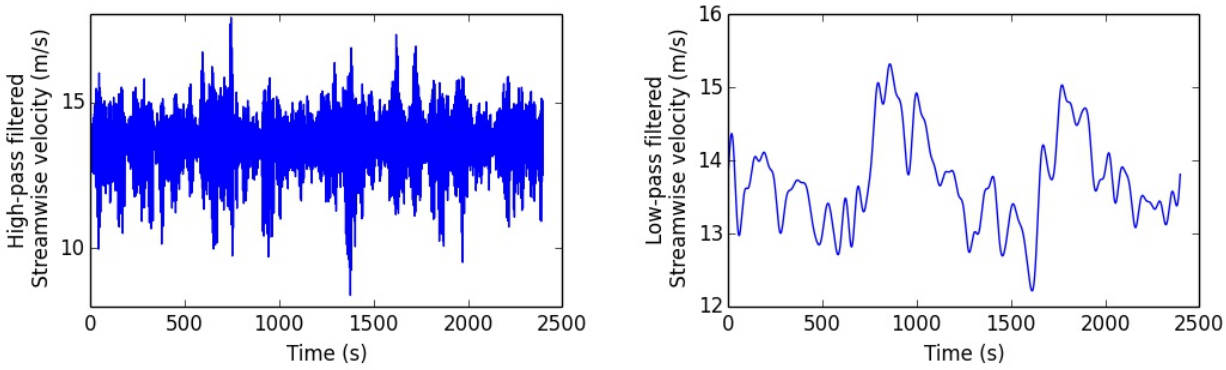

(a): High-pass filter $f > 0.5f_{BR}$ (b): Low-pass filter $f < 0.1f_{BR}$

Figure 5: Streamwise velocity at the 75% span of a hypothetical NREL 5MW turbine in a day time ABL analyzed using a low-pass and a high-pass filter.

Figure 3 shows a plot of the streamwise velocity as experienced by a point at the hub height and at 75% span on a hypothetical NREL 5MW turbine in a true day time ABL. This analysis is performed using data from the higher-resolution moderately convective boundary layer simulation in Table 2. A spectral analysis of the two velocity signals in Figure 4 shows that their frequency content is very similar to each other at low frequencies compared to the blade rotation frequency f_{BR}. Using a high/low pass filter, the velocity signal at 75% span location is split into two parts, viz., fluctuations with time scales larger than ten blade rotation time scales (low-pass filter - $f < 0.1f_{BR}$) and those with time scales smaller than two blade rotation time scales (high-pass filter $f > 0.5f_{BR}$). Figure 5 shows that the low-pass filtered signal is very similar to that at the hub height in Figure 3(b), while the high-pass filtered signal seems to be independent of the low frequency signal. A more refined band-pass filter analysis in Table 4 shows that the lower-end of the frequency spectrum contributes to most of the variance followed by the fluctuations around the blade rotation frequency, while the intermediate range contains very little energy.

We use this spectral gap to split further analysis of the ABL turbulence using what we call a "frozen turbine" and a "frozen turbulence" approximation. This is done to isolate the different effects that contribute to temporal variability in the turbulent atmospheric winds. The "frozen turbine" analysis ignores the rotation of the turbine and considers only effects of the advection of the energy containing eddies in the atmosphere through the wind turbine rotor. The "frozen turbulence" analysis does the opposite: it ignores the effect of the advection of the turbulence eddies and considers only the rotation of the turbine blade through "frozen" turbulence eddies.

Frequency band	Percentage of variance in frequency band
$0 < f < 0.1 f_{BR}$	62.84%
$0.1 f_{BR} < f < 0.5 f_{BR}$	2.12%
$0.5 f_{BR} < f < 1.5 f_{BR}$	24.34%
$1.5 f_{BR} < f < 2.5 f_{BR}$	6.68%
$2.5 f_{BR} < f < \infty$	5.54%

Table 4: Band-pass filter analysis of the stream-wise velocity measured at the 75% span location of a hypothetical NREL 5MW turbine in a day time ABL. The table shows the contribution of different frequency bands with respect to the blade rotation frequency f_{BR} to the total variance of the velocity signal.

III.A.1. "Frozen Turbine" Analysis

We first analyze the forcing on a wind turbine at low frequencies where the rotation of the blade is approximated to be irrelevant. The objective of this analysis is to quantify the time scales of the energy containing eddies in a day time atmosphere as experienced by modern commercial wind turbines. Vijayakumar et. al.[35] used a spatial filtering approach as shown in Figure 6 to compute the advection time scales of the energy containing turbulence structures in the ABL past a hypothetical NREL 5MW turbine. They concluded that the time scales of these structures were $\sim O$(multiple rotation times). Table 5 shows the results of the same analyses applied to the data generated by the LES of ABL in Section II.A. Lavely et. al.[13] have shown that the turbulence structures as defined in the previous analysis are very well correlated with the time response of wind turbine loads in the ABL.

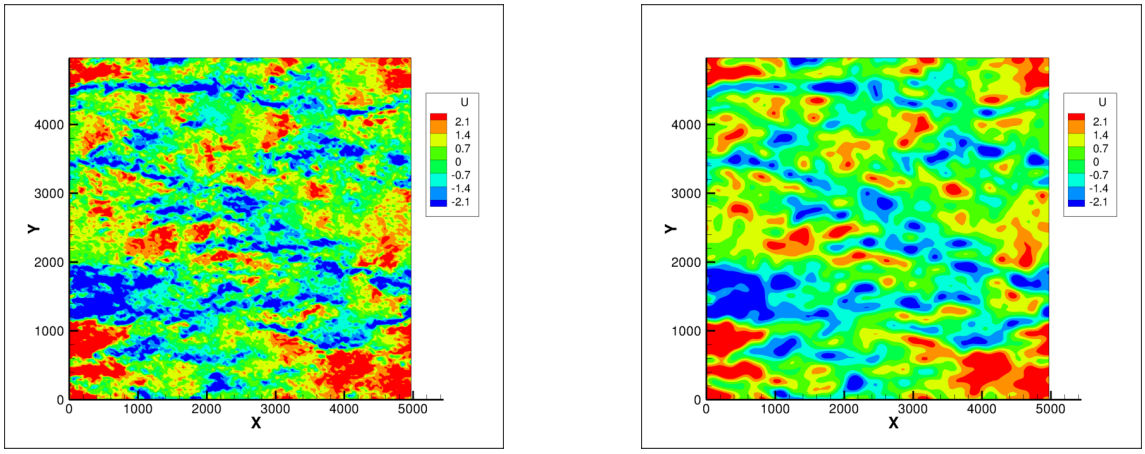

(a): Unfiltered (b): Filter cut off wavenumber=20

Figure 6: Contours of u' (a) unfiltered and (b) filtered using a low-pass filter retaining the energy-containing scales at hub height (z=90m).

	Low speed streaks	High speed streaks
Time Scale	0.78 minutes ($\sim 9 rotations$)	0.75 minutes ($\sim 9 rotations$)
	Updrafts	Downdrafts
Time Scale	0.47 minutes ($\sim 5 rotations$)	0.42 minutes ($\sim 5 rotations$)

Table 5: Advective time scales of eddies defined using streamwise and vertical velocity fluctuations at hub height (z=90m) of the NREL 5MW wind turbine for a particular choice of filter cutoff and threshold levels using the more highly resolved ABL simulation in Table 2.

Many research publications increasingly suggest the use of LIDAR based feed-forward control of the pitch and the rpm of wind turbines to optimize power capture and alleviate load fluctuations. The knowledge of

the structure of ABL turbulence and the time scales of the large-eddy structures from the current analysis (Table 5) could be potentially used to help optimize wind turbine control systems. The response of such a control system is likely to be most useful when the ABL structure near the wind turbine changes from a low speed streak to a high speed streak or vice versa.

III.A.2. "Frozen ABL" Analysis

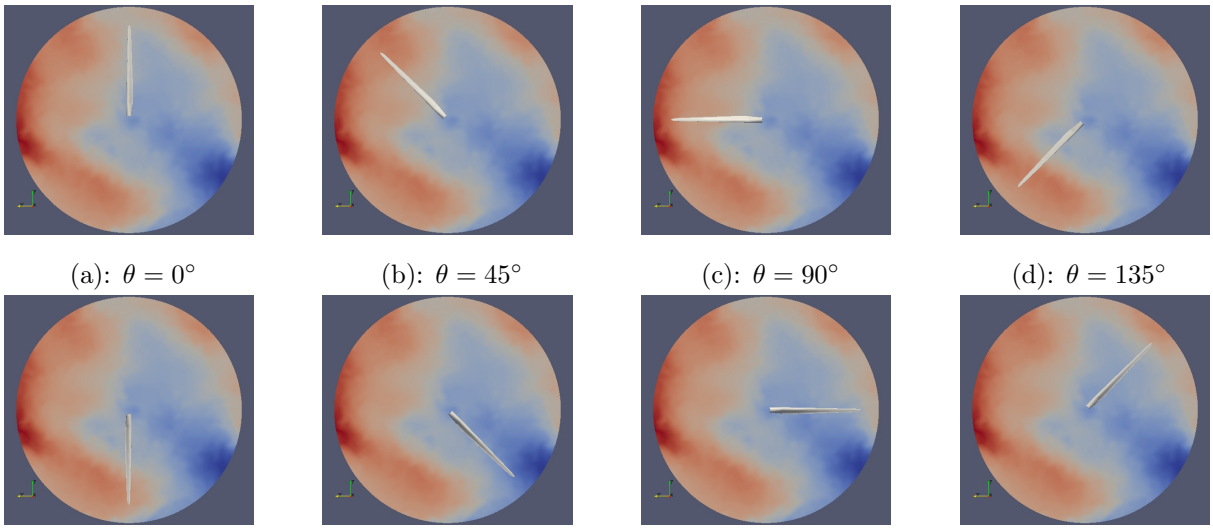

(a): $\theta = 0°$ (b): $\theta = 45°$ (c): $\theta = 90°$ (d): $\theta = 135°$

(e): $\theta = 180°$ (f): $\theta = 225°$ (g): $\theta = 270°$ (h): $\theta = 315°$

Figure 7: Illustration of fluctuations experienced by a hypothetical NREL 5MW turbine blade rotating through a frozen ABL. The colored contours represent the fluctuations in the streamwise velocity component in a day time ABL (Dark Red - 17m/s and Dark Blue is 10m/s.)

While the largest energy containing eddies of the ABL cause fluctuations in wind turbine loads over multiple rotation time scales, the individual turbine blades are forced at the higher frequencies as the blades rotate through turbulence structures with subrotation time scales as shown in Figure 7. To quantify the fluctuations experienced by a turbine at frequencies greater than the blade rotation frequency, we freeze the ABL at a single time and analyze the azimuthal spectra of the velocity at different radial stations by taking advantage of the horizontal homogeneity. This type of analysis could be thought of as being similar to Taylor's frozen turbulence approximation.[57] The current analysis method rotates a hypothetical turbine blade in a frozen ABL, while the conventional application of Taylor's approximation advects a frozen turbulence field past the measurement point at a prescribed velocity. The horizontal homogeneity of the ABL is used to average the azimuthal spectra over several disks spread across the $5km \times 5km$ horizontal domain. The current analysis is performed using data from the higher-resolution moderately convective boundary layer simulation in Table 2. In Figure 8, we plot the azimuthal spectra of streamwise velocity fluctuations and the resultant *Local Flow Angle* at different radial sections of a NREL 5MW turbine in a day time ABL using the "frozen ABL" analysis. This shows that the energy in azimuthal fluctuations of the streamwise velocity increases from near the hub ($r = 5m$) towards the tip of the blade ($r = 55m$). It is apparent from Figure 8 that the dominant forcing is at the blade rotation frequency at all spanwise locations and becomes negligible at frequencies greater than four times the blade rotation frequency. A turbine blade experiences the effect of these fluctuations through the changes in the local angles of attack as it sweeps through the internal turbulent eddy structure. The true angle of attack on a blade section is affected by the reduction of the average velocity in the average streamtube preceding the turbine rotor. Because this induction effect is not included in our "frozen turbulence" analysis, the computed angle of the flow relative to the hypothetical chord line of a NREL 5MW blade section is called a *Local Flow Angle*. Figure 8, which includes the spectra of the *Local Flow Angle* as well, shows that the variability in the *Local Flow Angle* is also highest at the blade rotation frequency and reduces at higher frequencies. Figure 9 shows a profile of the standard deviation of streamwise velocity fluctuations and the resultant *Local Flow Angle* against the radial location. Figures 8 and 9 suggest the potential importance of temporal local flow angle variations on sectional load fluctuations.

They also show that the effect of the streamwise velocity fluctuations on the *Local Flow Angle* is the highest around 30% of the blade radius and reduces towards the tip. This result indicates that the middle part of the blade is likely to experience significant transient separation while operating in a true ABL.

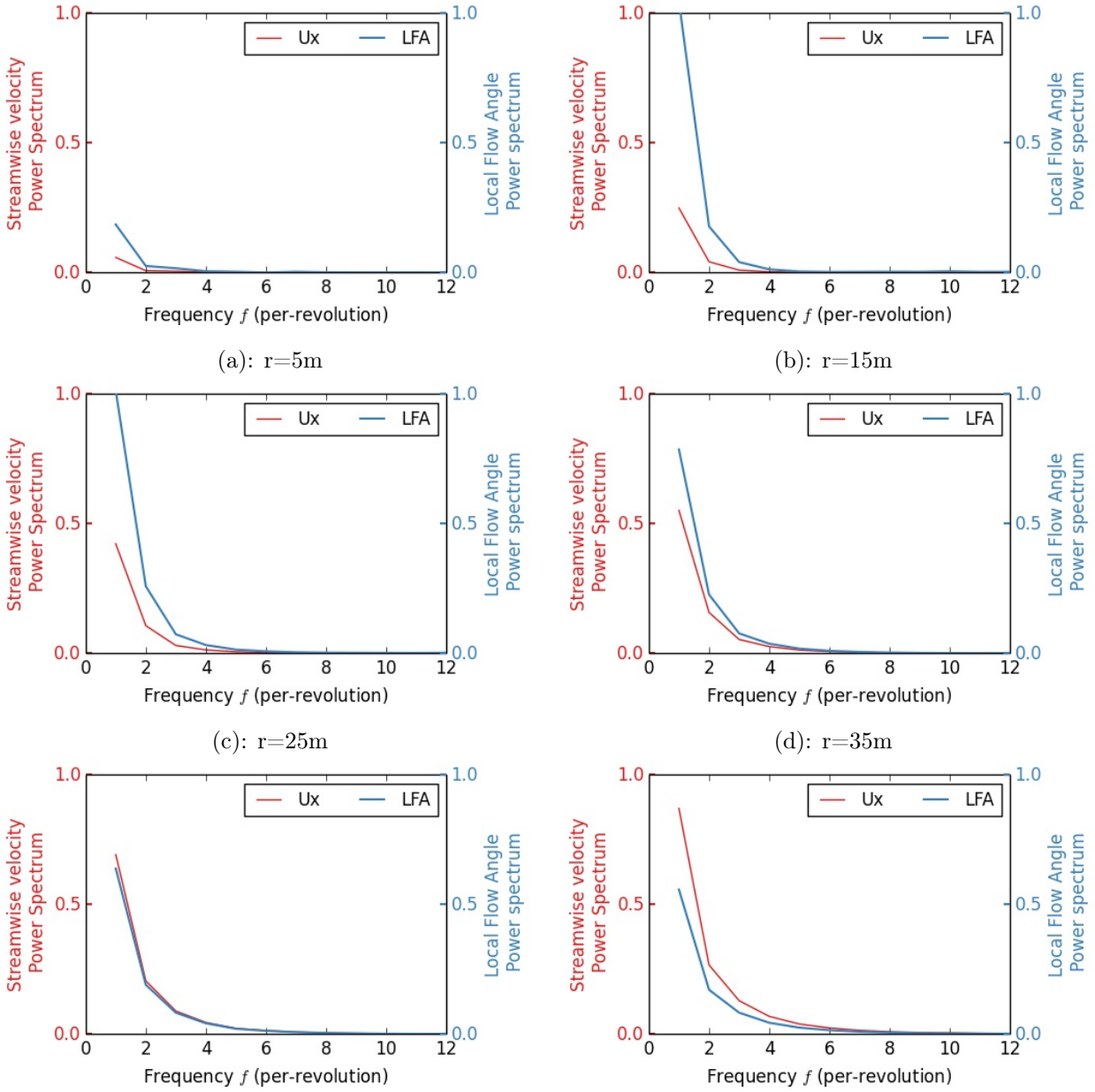

(a): r=5m (b): r=15m

(c): r=25m (d): r=35m

(e): r=45m (f): r=55m

Figure 8: Azimuthal spectra of streamwise velocity fluctuations and the resultant *Local Flow Angle* at different radial sections of a NREL 5MW turbine in a day time ABL.

III.B. Choice of Spatio-Temporal Location of the Wind Turbine in the ABL Domain

The highly resolved CFD of the flow around a three bladed rotor is computationally very expensive and cannot be run until converged statistics are obtained. Lavely et. al.[17] have shown that the averaging time required to obtain converged blade load statistics in a realistic ABL is longer than 30 minutes. The advective eddy time scales quantified in table 5 were used to choose appropriate times and locations when the wind turbine experiences large eddy turbulence structure passage in a reasonably short time interval. Figure 10

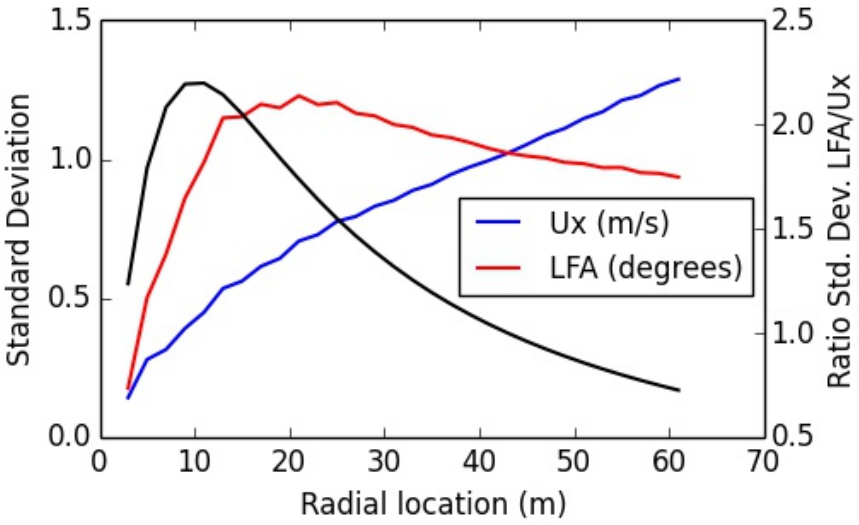

Figure 9: Profile of standard deviation of streamwise velocity fluctuations (Ux) and the resultant *Local Flow Angle* (LFA) on a hypothetical NREL 5MW turbine in a day time ABL. The black line shows the ratio of the two corresponding to the axis on the right.

shows isocontours of stream-wise velocity in the vicinity of the chosen wind turbine location. Observe, in the figure, a single rotating turbine blade during passage of a "low speed streak", a turbulence eddy with coherent lower-than-average horizontal velocity. The decision on the choice of location of the wind turbine in the ABL was made before many of the current analyses were performed. It is well known that the low speed streaks in the ABL are coherent and well correlated with the updrafts. This change in the flow angle with respect to the earth fixed co-ordinate system was expected to lead to large changes in the angle of attack on the wind turbine blades. Hence, the wind turbine in the *SRBIA* simulations was placed at the leading edge of a low-speed streak. Figure 11 shows isocontours of stream-wise velocity on a plane 10m in front of the chosen wind turbine rotor location.

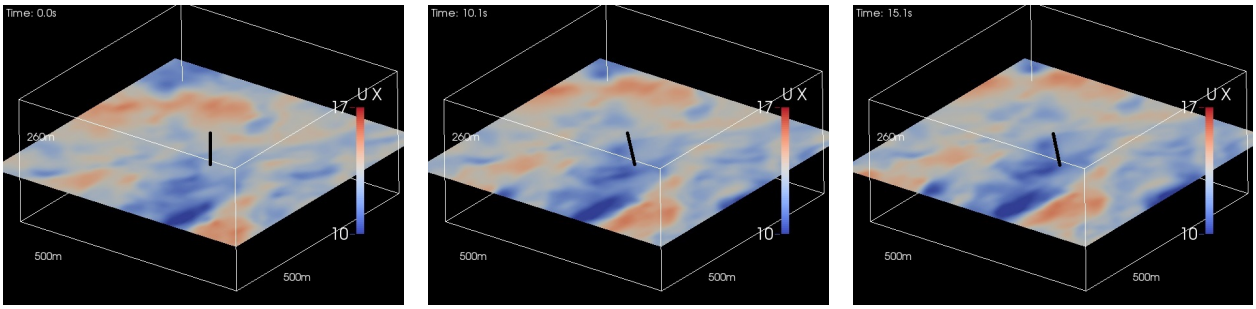

(a): t = 0s (b): t = 10.1s (c): t = 15.1s

Figure 10: Contour of stream-wise velocity around the choice of the wind turbine location in the ABL dataset.

III.C. Response of Integrated Blade Loads to ABL Turbulence

Figure 12 shows the time variation of integrated moments with disk-averaged horizontal velocity 10m upstream of the blade. The disk was chosen to be 10m in front of the turbine as it is greater than two chord lengths (max chord = 4.6m) and only $0.16R$ away ($R =$ turbine radius). The analysis in Table 6 shows that the power predicted by the simulation is consistent with the expected power for the average streamwise velocity on the rotor plane 10m preceding the turbine.

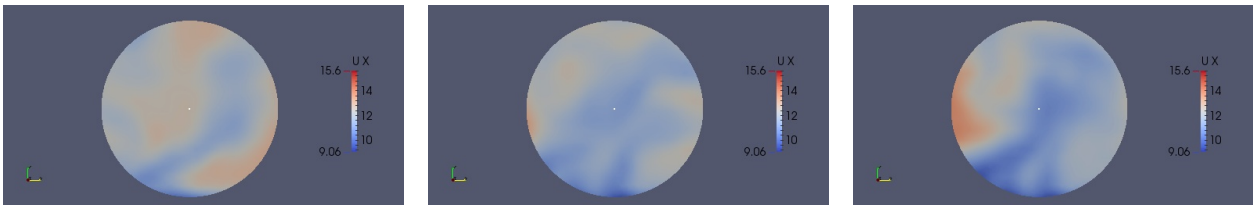

(a): t = 0s (b): t = 10.1s (c): t = 15.1s

Figure 11: Stream-wise velocity on a disk 10m in front of the blade from the ABL dataset.

Average Torque over 2 revolutions	$821kNm$
Average Streamwise velocity on disk over 2 revolutions	$11.53m/s$
Average Power over 2 revolutions at 12 rpm	$1.03MW$
Expected Average Power for 3 blades	$\approx 3MW$
Expected Power for NREL 5MW turbine at $14m/s$ and 8.7° pitch	$5MW$
Expected Power for NREL 5MW turbine at $11.53m/s$ and 8.7° pitch with approximately same power coefficient	$2.79MW$

Table 6: Verification of SRBIA results using approximate analysis.

Figure 12(a) shows that disk-averaged streamwise velocity 10m preceding the blade changes by only 1-2% (0.15m/s) over the 9s time period, while the disk-averaged vertical velocity fluctuates with a frequency of 1 per-rev by $\pm 1m/s$. This fluctuation of the vertical velocity is likely due to mixing induced by the single bladed turbine and is observed in the span-wise velocity as well.

Figure 13 shows two rapid reductions in torque and two less rapid increases creating sub 1 per-rev variations in torque that over 40% of the mean over the 9s period of simulation. These relatively rapid load responses reflect internal variations in eddy structure. Note that the low speed streak passing through the rotor disk does not occupy the full disk area preceding the rotor. Thus the blade experiences a downward ramp in torque as it cuts through the eddy structure and recovers the torque as it passes through the low speed streak. The change in the torque due to this structure is $\sim 400kNm$ —roughly 40% of the mean torque over this time period. Control systems likely can not react to such large changes in torque over such short time periods. Figure 12(b) shows that the out of plane bending moment undergoes similar ramps over the same time periods. As a single blade in a three bladed rotor, the low speed shaft will respond with large out-of-plane bending moments due to rapid changes in asymmetries in the moments from the three blades. These rapid shifts in the out of plane bending moment might affect the fatigue life of the gear box and shaft bearings. The correlation in ramp pattern in torque and bending moment with the blade passage through low-speed eddy is repeated from $t = 10.8 - 13.8s$ as shown in Figure 14.

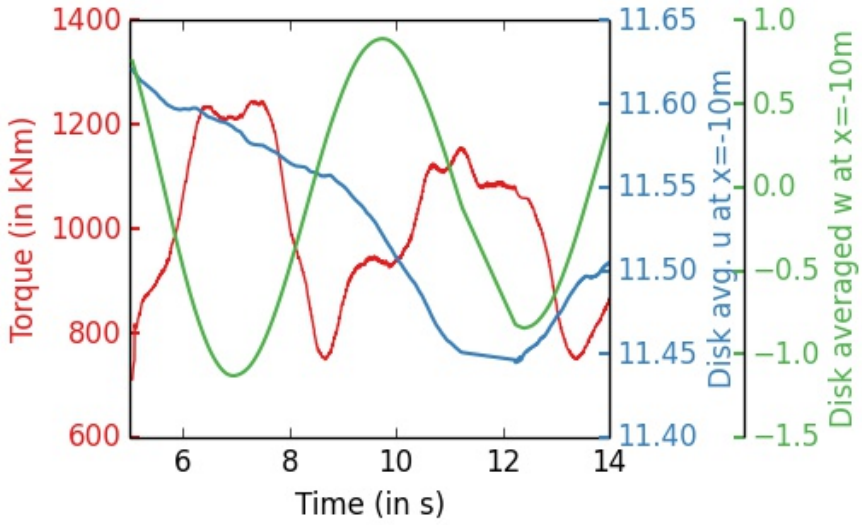

(a): Torque

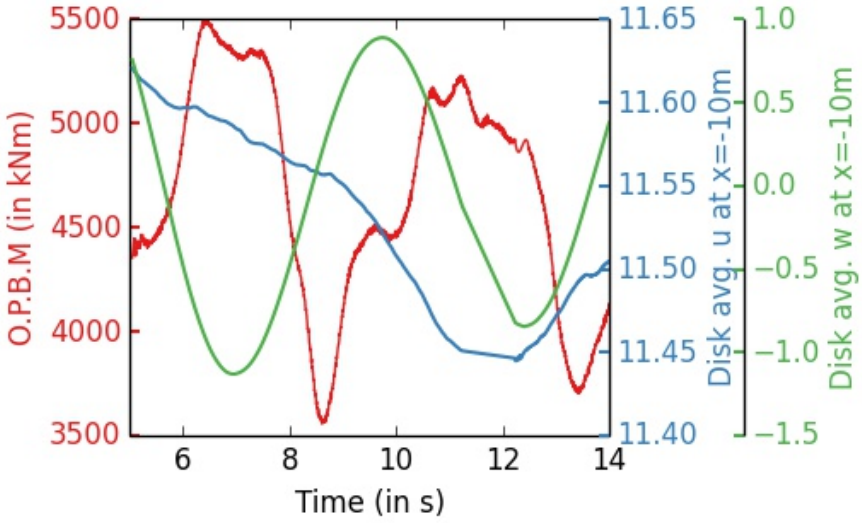

(b): Out of Plane Bending Moment

Figure 12: Correlation of integrated loads with the disk averaged stream-wise and vertical velocity 10m ahead of the rotor plane.

To further investigate blade moment fluctuations, the frequency spectrum of the integrated moments and the disk-averaged velocities are plotted in figures 15(a)-15(b) non-dimensionalized by blade rotation frequency. The vertical velocity spectrum contains a peak at the blade rotation frequency f_{BR}. The streamwise velocity spectrum, however, contains very little energy relative to the vertical velocity spectrum and only at the scales below the blade rotation frequency. Most of the energy in the torque spectrum is around the blade rotation frequency. To isolate the 1 per-rev content, we apply a low, high and a band-pass filter surrounding f_{BR} to the blade moments and disk-averaged velocity spectrum in front of the blade and plot the variations in the following three regions below:

- $< BR$ - $f < f_{BR}$ (low-pass filter)
- $\sim BR$ - $f \sim f_{BR}$ (band-passed between the dashed lines in figures 15(a)-15(b))
- $> BR$ - $f > f_{BR}$ (high-pass filter)

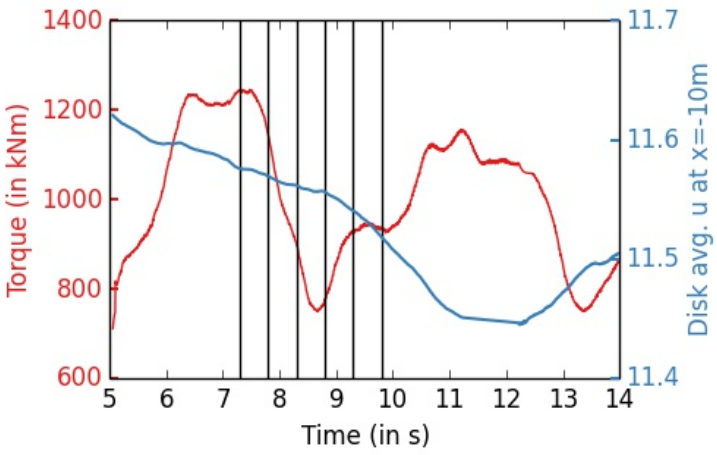

(a): Torque

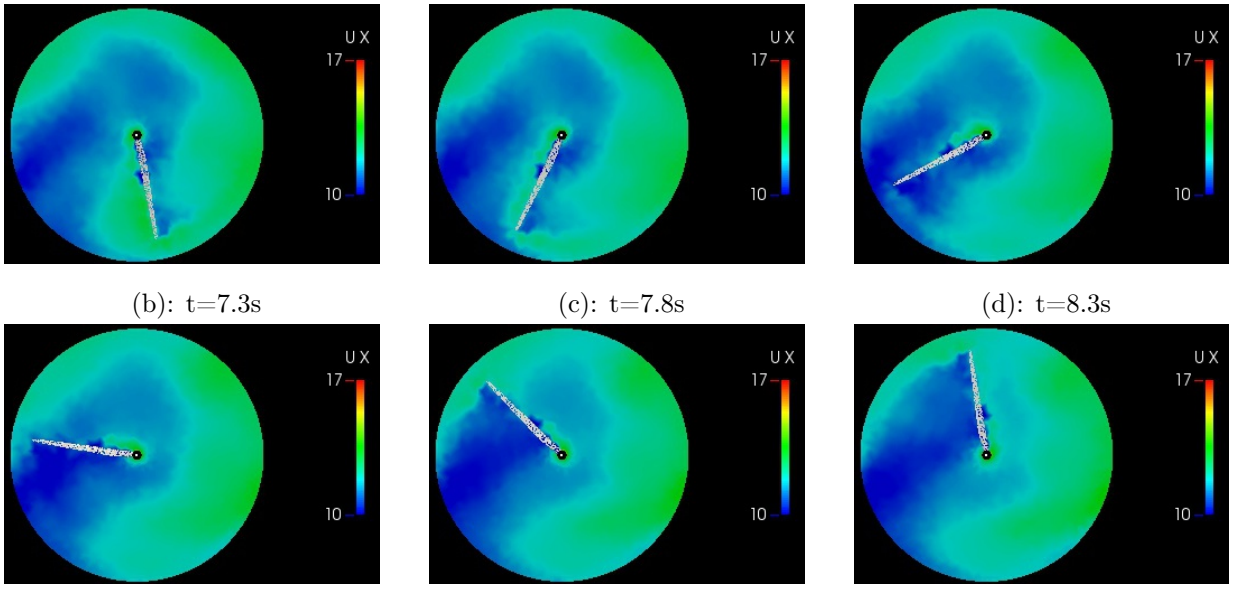

(b): t=7.3s (c): t=7.8s (d): t=8.3s

(e): t=8.8s (f): t=9.3s (g): t=9.8s

Figure 13: Correlation of the downward ramp in torque and it's recovery as the blade cuts through low speed streak from $t = 7.3 - 9.8s$. Figures (b)-(g) show contours of the streamwise velocity at different times on a plane 2m in front of the turbine.

The low-passed, band-passed and high-passed signals for the torque, out of plane bending moment, and the disk-averaged streamwise velocity are shown in Figure 16. We find that whereas the disk-averaged streamwise velocity contains relatively little variation at frequencies lower than the blade rotation frequency, the torque responds mostly at or above the blade rotation frequency. In Figure 17, we plot the contribution of each frequency band to the total variance (i.e., the area under the spectrum in each frequency band). Figure 17 indicates that the frequencies around and greater than the blade rotation frequency contribute over 99% of the total variance. This result is in contrast to the analysis by Lavely et. al.,[17] where they found that the frequency band lower than the blade rotation frequency contributes most of the variance. However, it is important to keep in mind that, while the advective time scales of the energy-containing eddies is multiple rotation times, the total time of the simulation is only 9s, just under two rotation times. If *SRBIA* were carried out for a longer duration, the relative contribution of the time-scales larger than blade rotation time scale to the total variance is likely to increase.

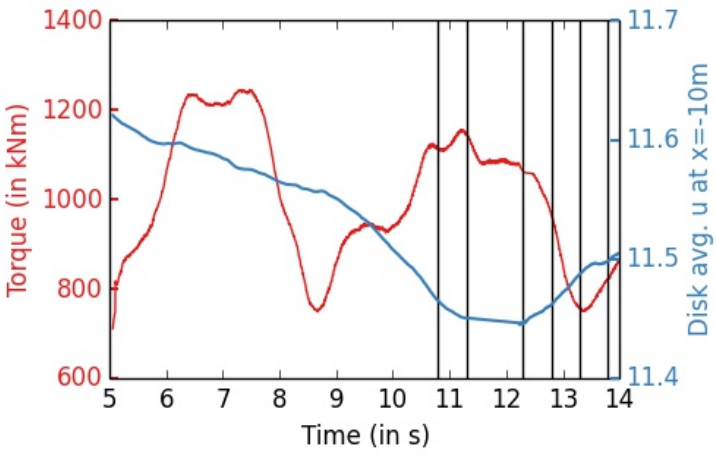

(a): Torque

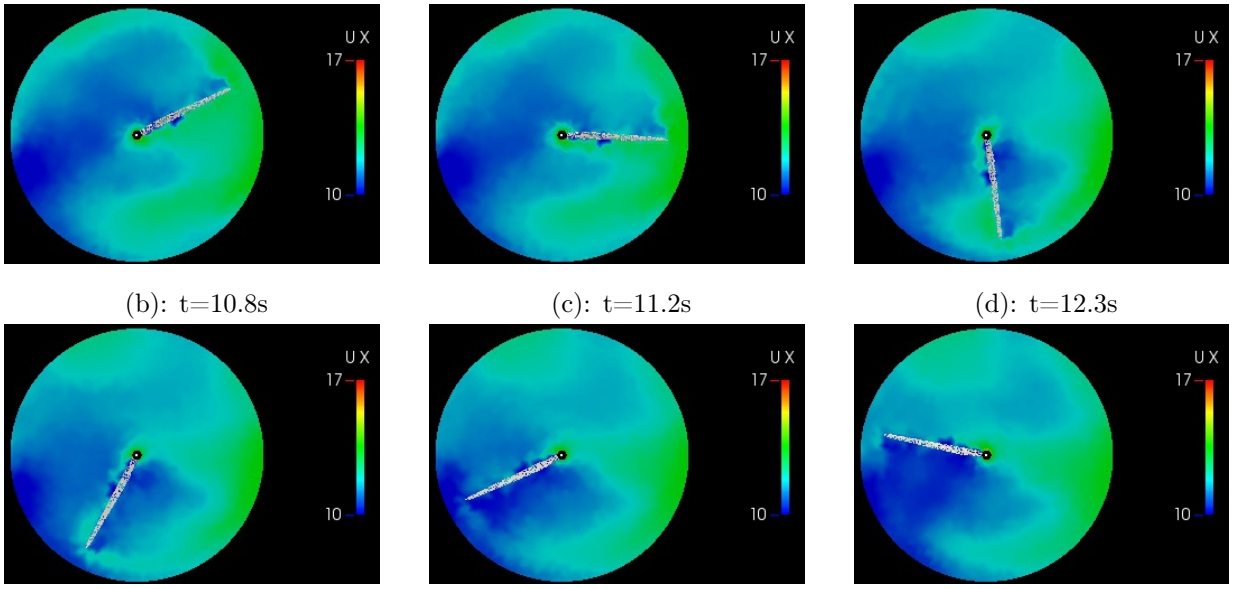

(b): t=10.8s (c): t=11.2s (d): t=12.3s

(e): t=12.8s (f): t=13.3s (g): t=13.8s

Figure 14: Correlation of the downward ramp in torque and its recovery as the blade cuts through a low speed streak from $t = 10.8 - 13.8s$. Figures (b)-(g) show contours of the streamwise velocity at different times on a plane 2m in front of the turbine.

III.D. Which Parts of the Blade Contribute the Most to Temporal Moment Fluctuations?

To answer the question posed in the title to this section, the blade is split into 6 equal parts as shown in Figure 18. The integrated loads split into 6 sections are plotted in two ways. Figure 19(a) shows the contribution from the individual sections, while the individual contributions are stacked up to recover the total loads in Figure 19(b). These figures show that the outer sections contribute the most to the total torque and the out-of-plane bending moment.

In Figure 20, we plot the statistics of the sectional torque through a profile of the mean torque and standard deviation in Figure 20(a) and the percentage contribution of each section to the total mean torque in Figure 20(b). These figures show that the outer 3 sections as a unit contribute nearly 70% of the total torque. While this is not surprising, it is interesting to learn from Figure 20(a) that the outer 50% of the blade also contains the largest fluctuations in torque.

Figure 21 shows the split of the standard deviation of torque at each section into the 3 frequency bands. The $> BR$ frequency band dominates throughout the blade while the contribution of $< BR$ band is significant

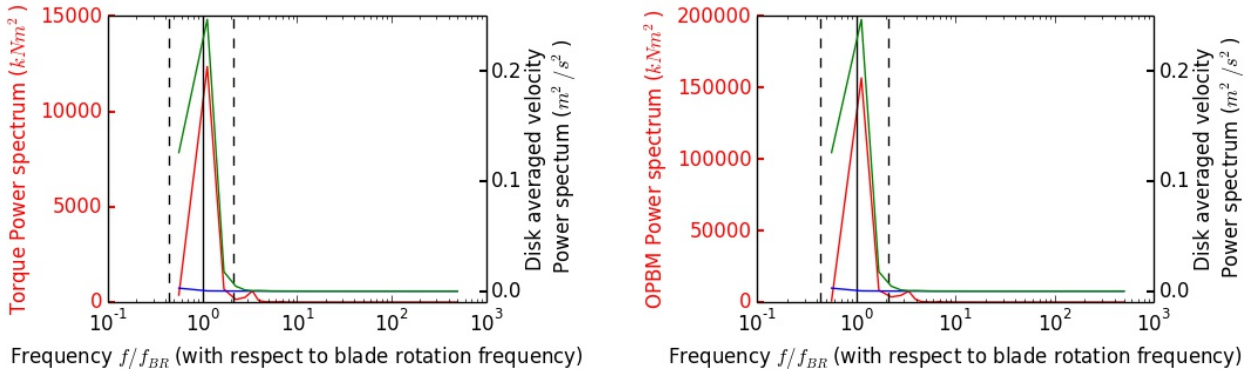

(a): Torque (b): Out of Plane Bending Moment

Figure 15: Spectrum of integrated torque and out-of-plane bending moment. Red line is integrated load, blue line is the disk-averaged u velocity and the green line is the disk-averaged w velocity in a plane 10m ahead of the wind-turbine. The frequencies are normalized on the blade rotation frequency f_{BR} shown with the black line.

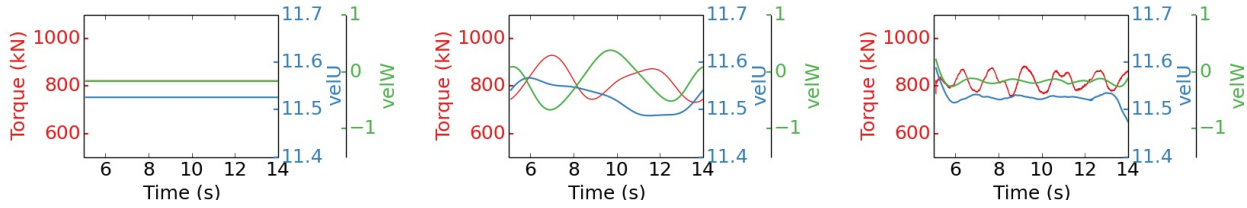

(a): Less than blade rotation (b): Near blade rotation (c): Greater than blade rotation

Figure 16: Variation of integrated blade torque and disk-averaged velocity in front of the blade filtered in the frequency regions $f < f_{BR}$, $f \sim f_{BR}$, $f > f_{BR}$ (see Figure 15).

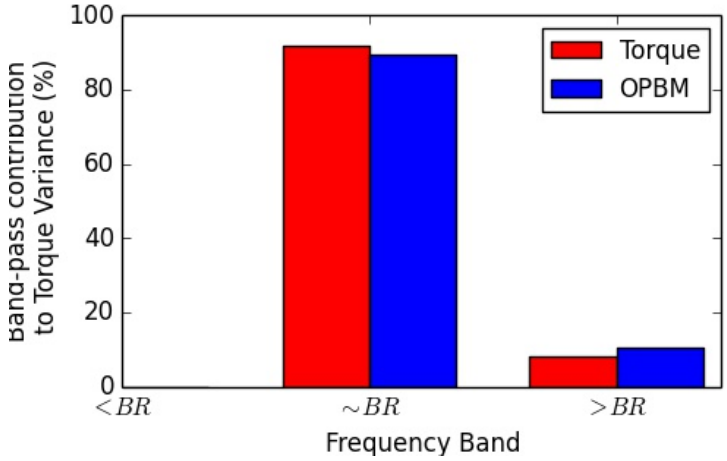

Figure 17: Percentage split of contribution to total load variance from each of the 3 frequency bands in Figures 15 and 16.

only in the first 4 sections.

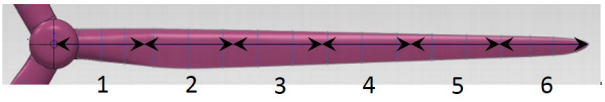

(a)

(b)

#	Range	Middle point	% span
1	0-10.5m	5.25m	8.3%
2	10.5-21m	15.75m	25.0%
3	21-31.5m	26.25m	41.7%
4	31.5-42m	36.75m	58.3%
5	42-52.5m	47.25m	75.0%
6	52.5-63m	57.75m	91.7%

Figure 18: Blade split into 6 sections

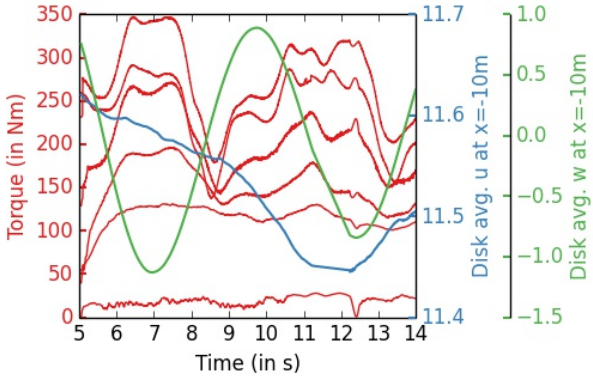

(a): Torque

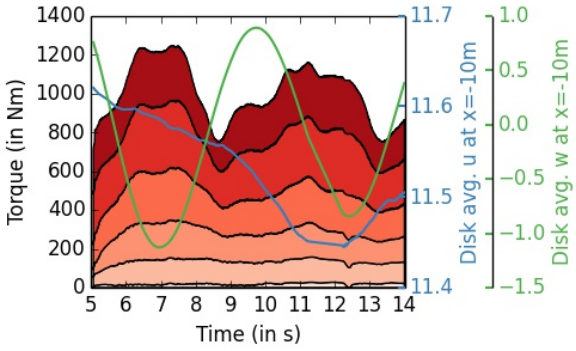

(b): Stacked Torque

Figure 19: Plot of sectional contributions to torque and out of plane bending moment.

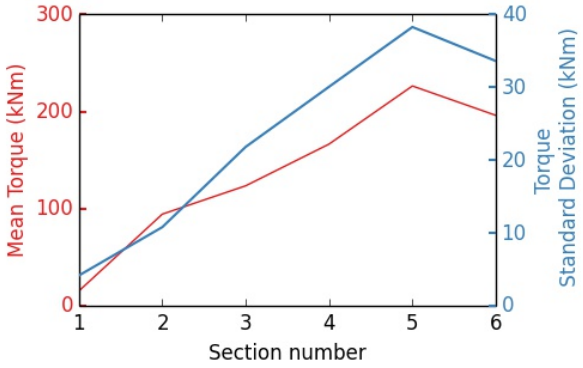

(a): Section wise mean Torque and Standard deviation.

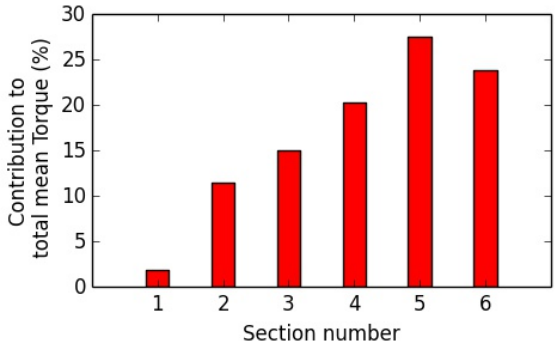

(b): Percentage contribution of each section to the total mean torque.

Figure 20: Sectional split of mean torque and standard deviation.

III.E. What Causes the Fluctuations in the Sectional Loads?

The analyses above indicate that the outer 50% of the blade contributes the most to torque variance at frequencies near and above the blade rotation frequency. The sectional load fluctuations could be attributed to a variety of different sources. Figure 22 shows a tree of all the possible causes of sectional load fluctuations on a turbine blade rotating in an ABL.

If the flow around each blade sectional is approximately two dimensional, the angle of attack on a section of the blade is an important parameter that controls the nature of the load fluctuations. Load fluctuations

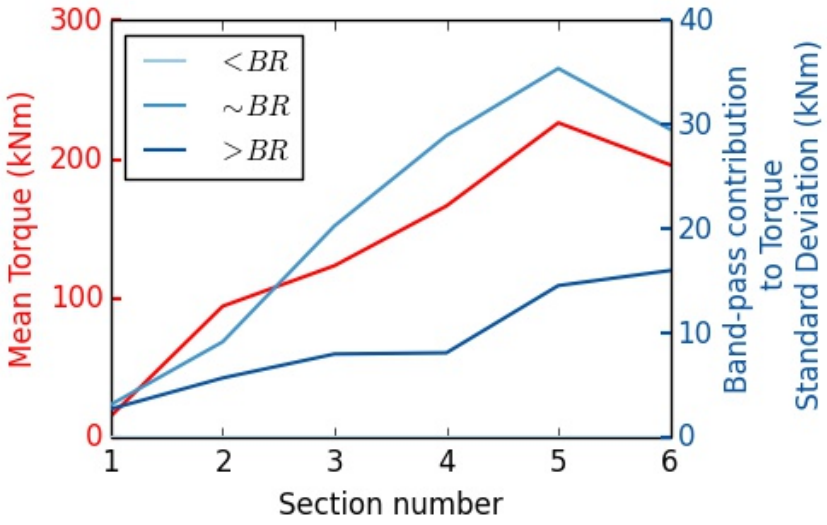

Figure 21: Band-pass contribution of each frequency band to standard deviation and variance of Torque at each section.

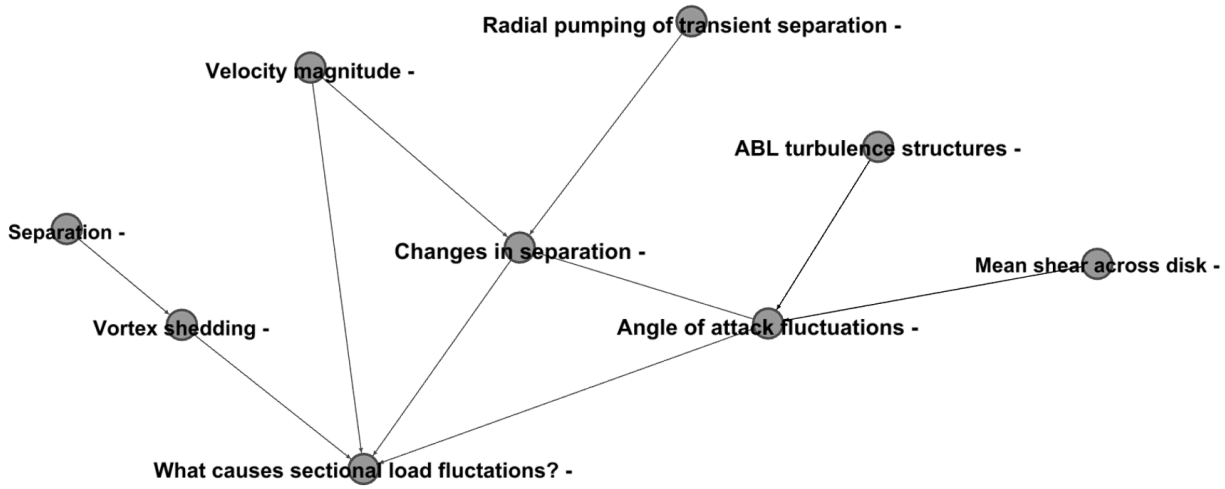

Figure 22: What causes sectional load fluctuations? - Possible answers

on an airfoil section can occur while the angle of attack is constant or varying in time. The details of the sectional load fluctuations under these two conditions is explained below.

- Constant Angle of Attack
  - Airfoil sections are known to experience large temporal fluctuations in loads relative to the mean when the angle of attack is close to or exceeds the static stall angle. Although the turbulent flow structures responsible for the load fluctuations are themselves highly unsteady, the angle of attack is constant with respect to time. The separation location may also change with time, although in a periodic manner. Periodic shedding of vortices from the separated boundary layer may also occur.
  - Another possible cause of sectional load fluctuations at a constant angle of attack is due to 3D effects. The separation from airfoil sections can cause neighboring airfoils sections to separate,

causing temporal fluctuations in the sectional loads. This is a known phenomenon in flows around rotating machinery like rotors, fans and turbines.[58]

- Changing Sectional Angles of Attack
  When the angle of attack changes with time, the loads are expected to fluctuate even in the linear regime of the $C_l - \alpha$ curve. When the angle of attack fluctuates around or exceeds the static stall angle, the airfoil section is expected to enter Dynamic Stall, generally with periodic vortex shedding within a dynamic stall cycle.

In summary the sectional load fluctuations can result from vortex shedding, temporal changes in separation and fluctuations in sectional angle of attack.

Estimating a Surrogate Angle of Attack on a Rotating Turbine in the ABL

While the angle of attack is an important parameter that controls the local blade boundary layer dynamics, its definition is not clear for a turbine blade rotating in an ABL. Guntur and Sorensen[59] have evaluated several existing methods to estimate the "angle of attack" in CFD simulations. However, the current methods cannot be applied to the case of a rotating turbine in an ABL because the flow into the turbine is not uniform and contains significant variability in the azimuthal direction (Figure 8).

Several experimental campaigns have been carried out to measure the aerodynamic characteristics of wind turbines in both controlled conditions (wind tunnels) and in the atmosphere (e.g.[60,61]) . Most of these campaigns use a five hole probe placed at an arbitrary location from the airfoil leading edge to determine the local flow angle and velocity magnitude. The five hole probes are calibrated under controlled conditions in a wind tunnel. Our analyses of the variation of the flow angle around airfoil sections in uniform inflow at a fixed angle of attack using 2D RANS simulations indicate that the placement of the five hole probes off the leading edge does not provide the most accurate flow angle that could approximate the angle of attack. Instead, we optimized the location of the probe to measure the best approximation of angle of attack in CFD simulations. The optimized probe location is then used to measure the flow angle relative to the local chord in *SRBIA* simulations. Since the flow angle obtained using this technique is not the true angle of attack (indeed it is not clear if an "angle of attack" is meaningful), the flow angle determined by this approach is referred to as the "*Surrogate Angle of Attack*". The magnitude of velocity at the same location is used as a surrogate to compute the instantaneous dynamic pressure.

Analysis of Sectional Load Fluctuations Using Surrogate Angle of Attack

To investigate the cause of the sectional load fluctuations, the correlation coefficient of torque force per unit span against the following three different quantities was plotted against radial distance along the blade:

1. *Surrogate Angle of Attack*
2. Velocity Magnitude
3. Distance from the leading edge of boundary layer separation on the suction side - Defined as the point when the chordwise shear stress changes sign.

The result plotted in Figure 23 shows that the torque force per unit span has a very high correlation with the *Surrogate Angle of Attack* (corr. coeff. ≈ 0.9) in the outer 70% of the blade. The separation point is negatively correlated in the outer 60% of the blade. Velocity magnitude, in contrast, is not well correlated with torque. Figure 24 shows the temporal relationships of sectional torque contribution and *Surrogate Angle of Attack* in each of the six sections defined in Figure 18(a). The progressive increase in the correlation with radial distance along the blade is apparent in Figures 24(a) - 24(f).

Figure 23 shows that the sectional correlation of torque with *Surrogate Angle of Attack* is much higher than with the velocity magnitude at that section. This strongly suggests that temporal fluctuations in loads are much more sensitive to changes in the *Surrogate Angle of Attack* than to velocity magnitude. The separation location is expected to move towards the leading edge of the airfoil section as the angle of attack increases. Consistent with this expectation, we find in Figure 23 that the torque force per unit span is negatively correlated with the separation location. The correlation of the torque force with the local velocity magnitude remains fairly low throughout the blade except near the root region. The tangential velocity due

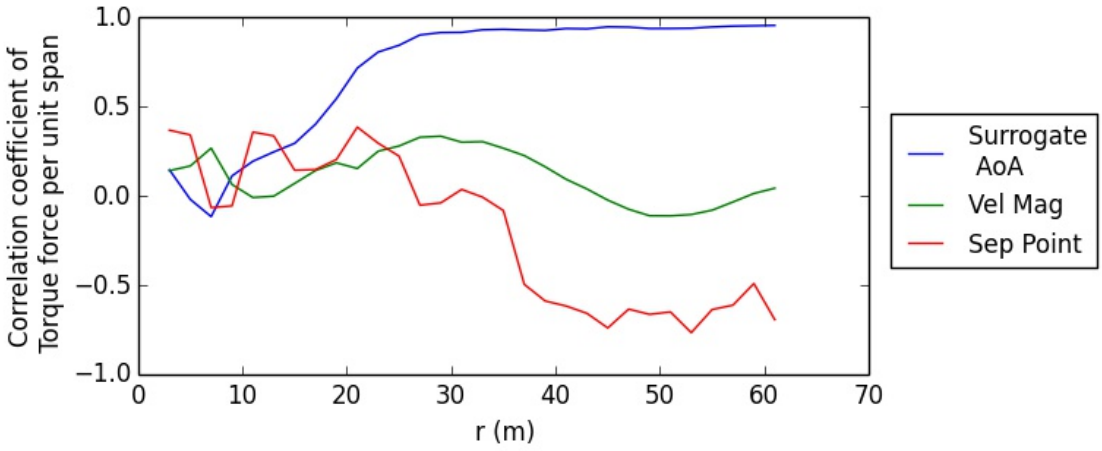

Figure 23: Correlation of Torque per unit span at different sections with the *Surrogate Angle of Attack* and the Velocity Magnitude.

to the rotation of the blade is either small or comparable to the streamwise velocity near the root. The airfoil sections near the root are expected to operate in the stalled region of the $C_l - \alpha$ curve. Hence, the sectional torque force is likely to be correlated better with the velocity magnitude in the inner regions compared to the outer 50% of the blade.

Based on the analysis above, further analysis of the sectional load fluctuations is split into the inner and outer 50% of the blade.

Analysis of the Sectional Load Fluctuations in the Outer 50% of the Blade

Figure 25 shows the radial/spanwise velocity around the blade using the same velocity as for the *Surrogate Angle of Attack*. We find that the radial velocity is significant compared to the tangential velocity only very close to the root. Based on this result, the flow around most of the airfoil sections of the blade is quasi-two dimensional especially in the outer 50% of the blade. While three dimensional effects may exist from blade rotation, Figure 25 suggests ABL turbulence does not contribute significantly over much of the blade.

Based on the previous observation, we compare the sectional loads at each airfoil section to its characteristics in 2D flow, an approximation used in lower order models such as BEM and ALM.[62] The torque force per unit span in the outer 50% of the blade is highly correlated with the *Surrogate Angle of Attack* as shown in Figures 26(a) - 28(a). The *Surrogate Angle of Attack* is also used to separate the local blade force into Lift and Drag components.

In Figures 26(b) - 28(b), we compare a scatter plot of the lift coefficient at select radial stations with the 2D lift polar used in BEM and ALM simulation for the NREL 5MW wind turbine.[1] In these figures, the engineering correction to the 2D $C_L - \alpha$ curve used to account for rotational augmentation is shown with dashed lines. We find that using the *Surrogate Angle of Attack*, the predicted loads in the outer 32% of the blade ($r = 43 - 61m$) compare well with the sectional lift characteristics and appear to be operating in the linear portion of the $C_L - \alpha$ curves of the corresponding airfoil sections. If these airfoils were instead operating around the non-linear stall region of the $C_L - \alpha$ curve, the sectional loads may not correlate well with the *Surrogate Angle of Attack*.

Based on the results of Figures 25-28, we make the following observations for the outer 32% of the blade.

- The radial/spanwise flow due to the ABL is small compared to the tangential flow at the *Surrogate Angle of Attack* location, suggesting that the flow is quasi-2D around each airfoil section.
- The torque force per unit span correlates extremely well with the *Surrogate Angle of Attack*.
- The airfoil sections are operating in the linear portion of the $C_L - \alpha$ curve.

Using these observations, we conclude that the sectional load fluctuations in the outer 50% of the blade are caused by the fluctuations in the *Surrogate Angle of Attack*.

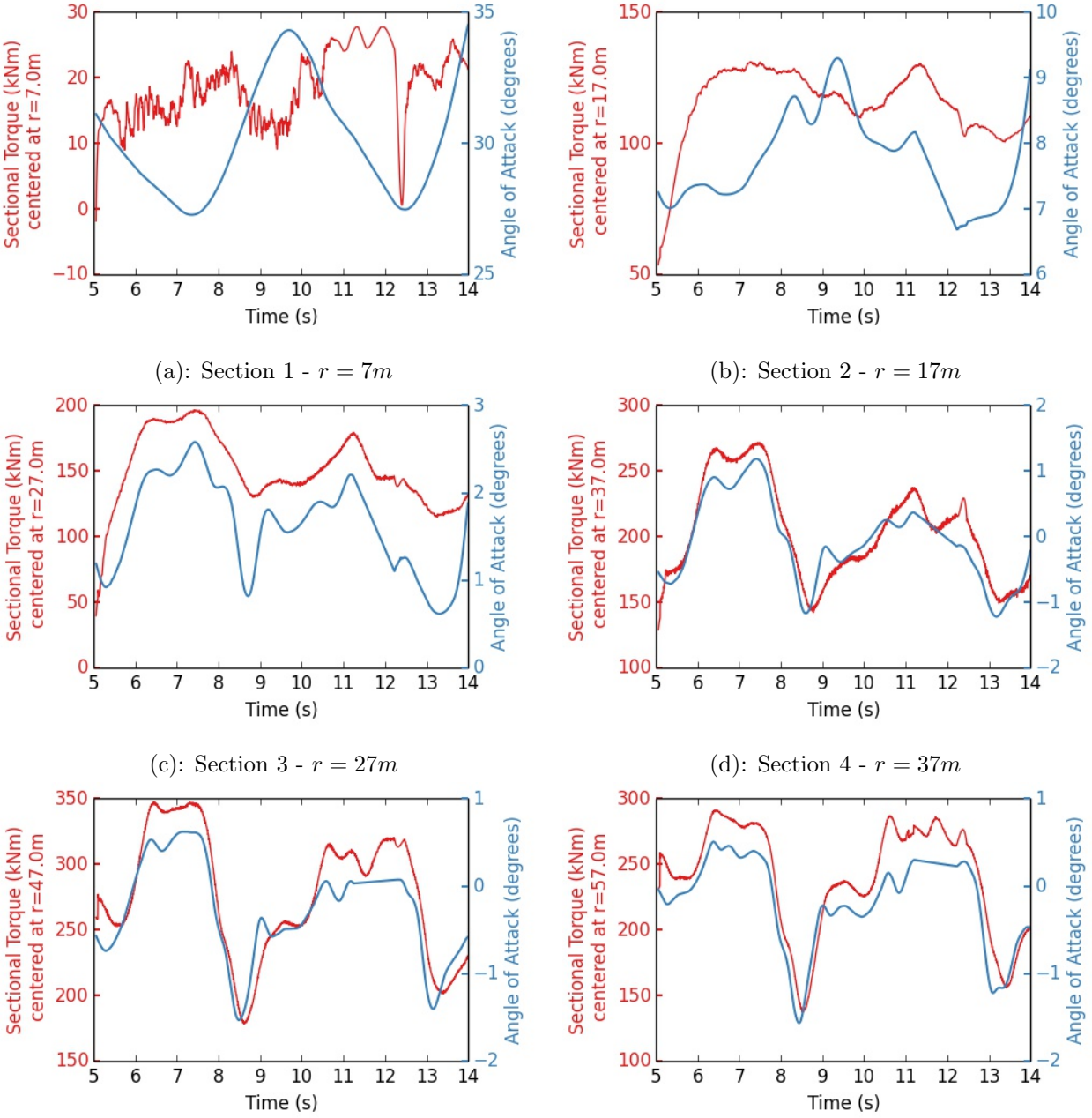

(a): Section 1 - $r = 7m$

(b): Section 2 - $r = 17m$

(c): Section 3 - $r = 27m$

(d): Section 4 - $r = 37m$

(e): Section 5 - $r = 47m$

(f): Section 6 - $r = 57m$

Figure 24: Temporal variation of sectional torque relative to section-averaged *Surrogate Angle of Attack*.

Analysis of the Sectional Load Fluctuations in the Inner 50% of the Blade

The following characteristics differentiate the physics of the sectional load fluctuations in the inner 50% of the blade compared to the outer sections.

- **Rotational Augmentation**
  The rotation of the blade causes the inboard airfoil sections to deviate from 2D characteristics more so than outer sections. Three dimensional flow patterns reduces the slope of the $C_L - \alpha$ curve at low angles of attack, but increases the static stall angle and the stall lift coefficient as shown by Guntur and Sørensen.[59] This phenomenon is known as "rotational augmentation"/"stall delay". The physics behind delayed stall from rotation augmentation is a subject of open investigation and is currently

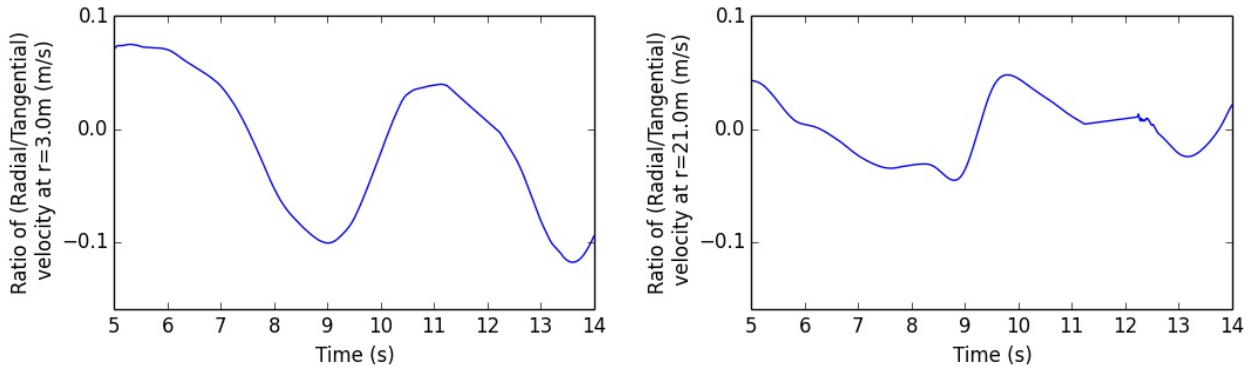

(a): r=3m

(b): r=21m.

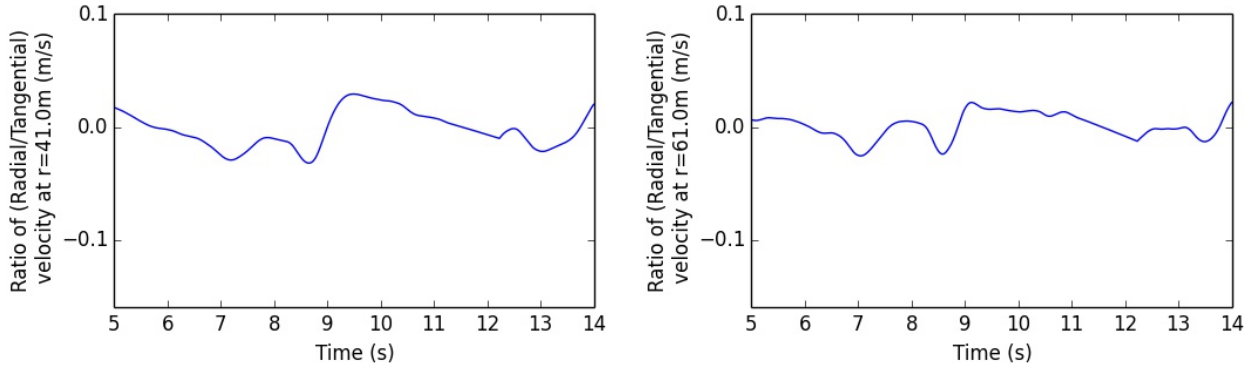

(c): r=41m

(d): r=61m.

Figure 25: Ratio of radial over tangential velocity at 4 blade locations.

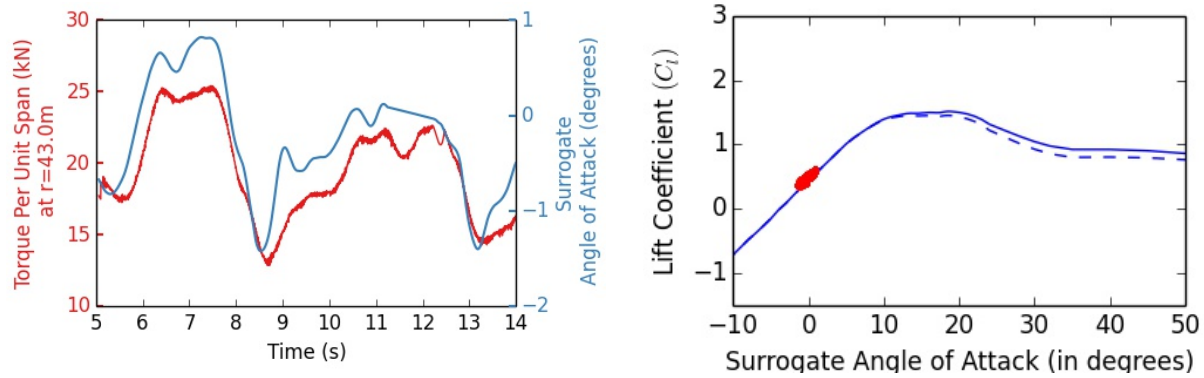

(a): Torque per unit span

(b): Location of the points on the $C_l - \alpha$ curve.

Figure 26: (a) Comparison of torque force per unit span with *Surrogate Angle of Attack*, and (b) scatter plot of $C_L - \alpha$ using the *Surrogate Angle of Attack* with the corresponding sectional lift polar at $r = 43m$.

attributed to factors such as strong radial flow in the separated regions (centrifugal pumping), modified laminar/turbulent transition etc. Modern commercial wind turbines take into account rotational augmentation and are designed to operate at a higher angle of attack in the inner sections compared to the outer sections.

- **Larger Fluctuations in the Angle of Attack compared to the outer sections**
  The inner sections of the blade are likely to experience larger temporal fluctuations in the Angle of Attack compared to the outer sections.

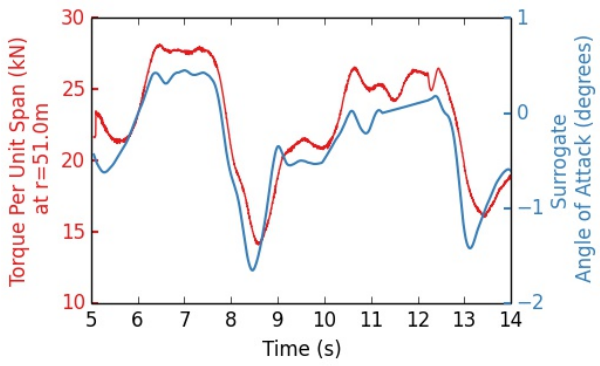

(a): Torque per unit span

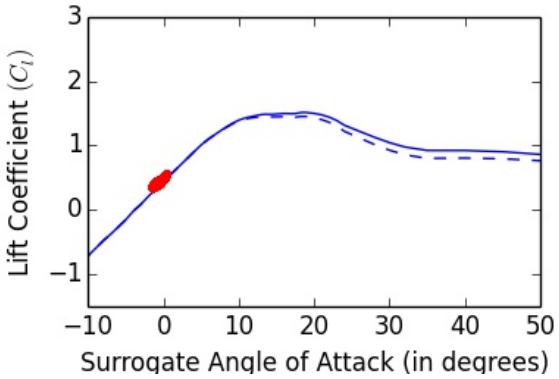

(b): Location of the points on the $C_l - \alpha$ curve.

Figure 27: (a) Comparison of torque force per unit span with *Surrogate Angle of Attack*, and (b) scatter plot of $C_L - \alpha$ using the *Surrogate Angle of Attack* with the corresponding sectional lift polar at $r = 51m$.

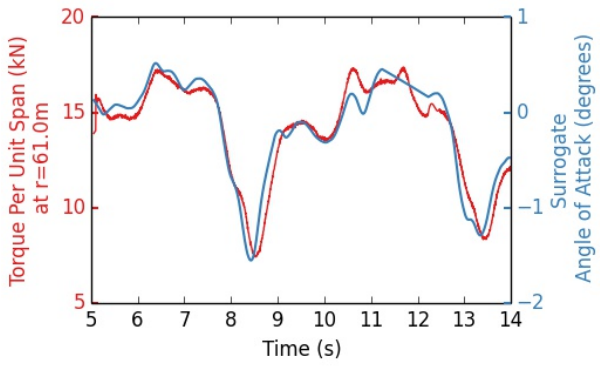

(a): Torque per unit span

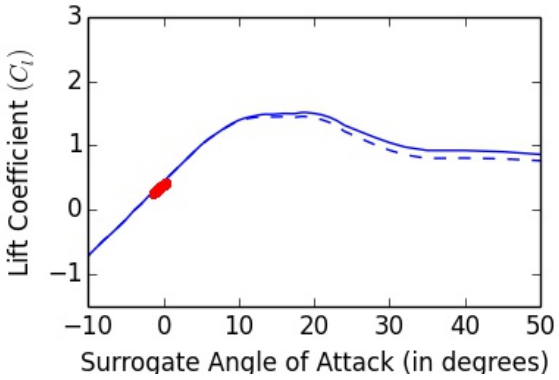

(b): Location of the points on the $C_l - \alpha$ curve.

Figure 28: (a) Comparison of torque force per unit span with *Surrogate Angle of Attack*, and (b) scatter plot of $C_L - \alpha$ using the *Surrogate Angle of Attack* with the corresponding sectional lift polar at $r = 61m$.

- **Unsteady Aerodynamics**
  Each airfoil section experiences fluctuations in flow angles at different time scales. The reduced frequency is the forcing frequency normalized by the advection time scale across half chord. This important parameter qualifies the level of unsteady aerodynamics on airfoil sections. When the reduced frequency is below ~ 0.05, the changes in the angle of attack are generally slow enough for the airfoil to respond in a quasi-steady manner. Unsteady aerodynamic effects become important when the reduced frequency exceeds ~ 0.05 and are strong above 0.2.[63] In Figure 29(a), we plot the reduced frequency against the radial location when forced at different frequencies with respect to the blade rotation frequency. Figure 29(b) shows the portion of the blade experiencing unsteady effects. These figures indicate that the inner 50% of the blade is likely influenced by unsteady aerodynamic effects even when forced at the blade rotation frequency. The unsteady aerodynamic effects become particularly significant when the forcing frequency is two or four times the blade rotation frequency.

- **Dynamic Stall**
  A combination of large fluctuations in the angle of attack and higher reduced frequency creates ideal conditions for dynamic stall in the inner 50% of the blade. Dynamic stall creates a non-linear hysteresis loop in the loading pattern for a given oscillation in the angle of attack.[64] A large vortex develops on the suction side and is advected downstream causing large fluctuations in pressure and the resultant loads.

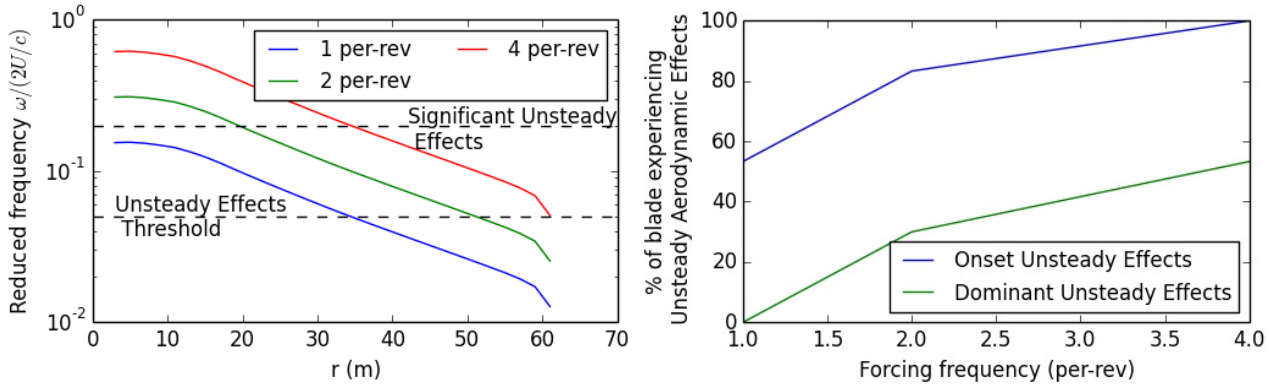

(a): Reduced frequency vs. Radial location

(b): Percentage of blade experiencing unsteady aerodynamic effects

Figure 29: Reduced frequency analysis of the flow around a NREL 5MW turbine showing the effect of unsteady aerodynamics.

Having reviewed sources of unsteady behavior, we focus here in related analysis using *SRBIA*. Figures 30-32 show the temporal relationship between torque force per unit span and the *Surrogate Angle of Attack* progressively drops as one moves towards the blade root. The mean *Surrogate Angle of Attack* also increases near the blade root as expected. Figures 30(b)-32(b) show the predicted lift coefficient on the $C_L - \alpha$ curve using the *Surrogate Angle of Attack* at the corresponding sections along with it's 2D characteristics. The engineering correction to the 2D $C_L - \alpha$ curve to account for rotational augmentation is shown in dashed lines. The correspondence between the prediction and the 2D polars get worse towards the root. The phenomenon of Rotational Augmentation is also observed in *SRBIA* through a reduction in the $C_L - \alpha$ slope from 17-46% of the blade (Figures 31(b)-30(b)) and a stall delay from 10-17% of the blade (Figure 32(b)). The current results suggest that these fluctuations do not cause any significant dynamic stall. This is likely due to the nature of the fluctuations observed in the limited time period of the simulation.

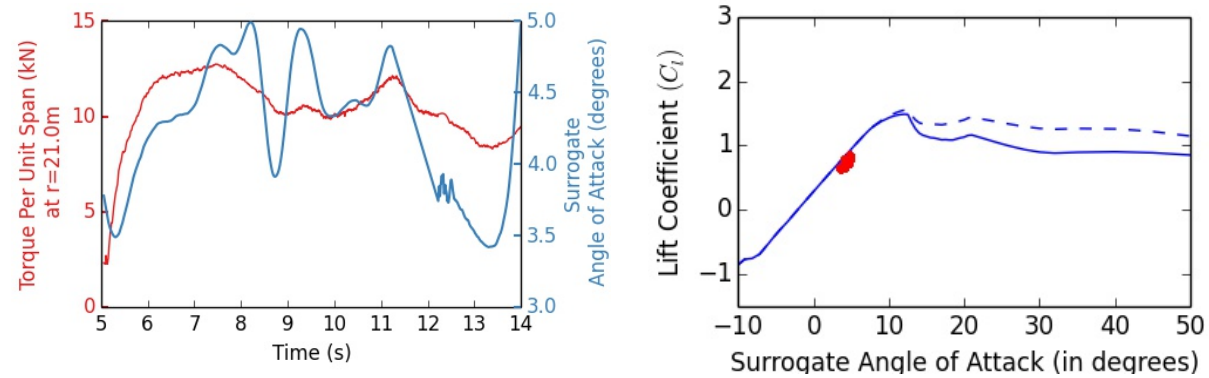

(a): Torque per unit span

(b): Location of the points on the $C_l - \alpha$ curve.

Figure 30: Comparison of torque force per unit span at $r = 21m$ with *Surrogate Angle of Attack*.

III.F. Analysis of Flow Separation in SRBIA

As discussed in Section II.C, the grid was designed, in part, to test the hypothesis that unsteady 3D separation of the blade boundary layer is important to the response dynamics of the wind turbine to atmospheric turbulence. While no clear definition of separation exists for 3D unsteady boundary layers,[65] here we define the separation point on an airfoil section as the location of the first negative shear stress along the chordline and in the chordwise direction. As shown in Figure 23, the separation location is indeed found to be unsteady in *SRBIA* and well correlated with the unsteady loads at each radial station. Figure 33 shows

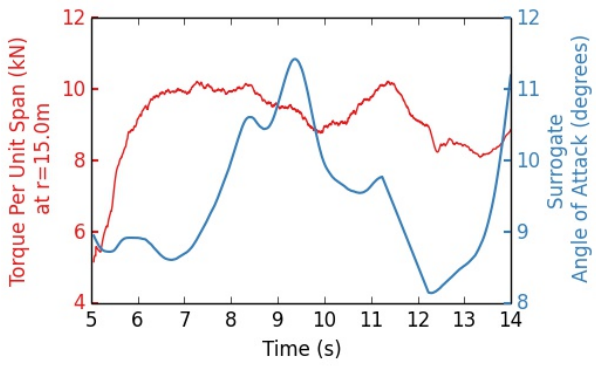

(a): Torque per unit span

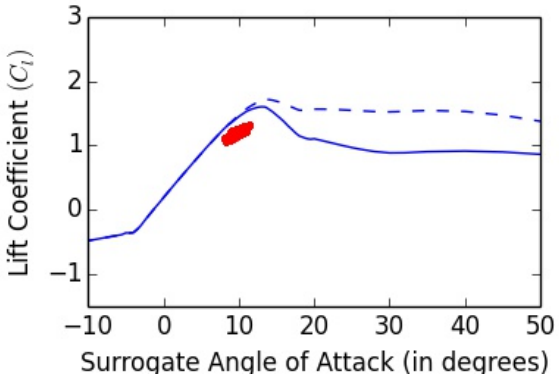

(b): Location of the points on the $C_l - \alpha$ curve.

Figure 31: Comparison of torque force per unit span at $r = 15m$ with *Surrogate Angle of Attack*.

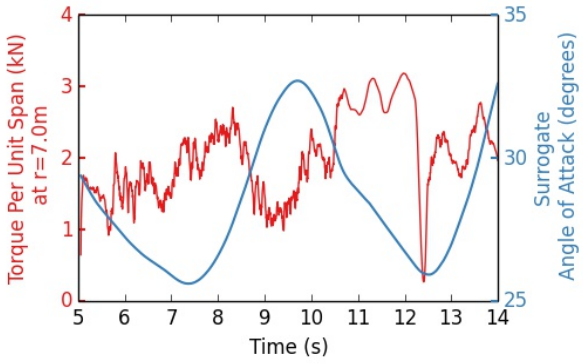

(a): Torque per unit span

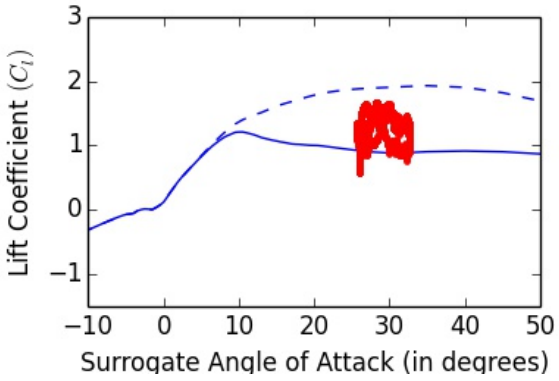

(b): Location of the points on the $C_l - \alpha$ curve.

Figure 32: Comparison of torque force per unit span at $r = 9m$ with *Surrogate Angle of Attack*.

a plot of separation streamlines at an instant in time with the red regions indicating separated or reverse flow. The flow around the blade is found to be separated, even if only mildly, along the entire blade. This observation is in contrast to the expected behavior as the flow was established to be fairly two-dimensional in the outer parts of the blade.

The separation throughout the blade is attributed to a combination of the gradient limiters, blended turbulence model and the flux differencing scheme in the calculation. This behavior was reproduced in a simpler configuration of a flow past a NACA-64 airfoil at 4° angle of attack in a day time atmospheric boundary layer. Figure 34 shows that the unsteady solver does not predict flow separation in uniform inflow, while considerable flow separation is predicted for the airfoil in an atmospheric boundary layer. The reason for this disparity is a subject of ongoing research and is not addressed further in this work. It is expected that the absolute location of the separation point may or may not be predicted accurately as there is not available experimental data for validation. However, the response of the separation point to fluctuations in the angle of attack is still expected to yield useful insight into the boundary layer dynamics.

The observed standard deviation of the separation location in SRBIA is consistent with the expected behaviour as shown in Figure 35. While the inner sections near the root experience large angles of attack nd are mostly insensitive to any local flow angle fluctuations, the outer sections experience low angles of attack and hence are not expected to experience much separation. The middle sections experience larger fluctuations in the flow angle compared to the other parts and are hence expected to also have larger fluctuations in the separation location.

Figure 36 shows the correlation coefficient of the time history of the separation location between adjacent radial stations. The blue curve shows the correlation coefficient without any time delay. Acording to Schreck et. al.[66] , the separation point is expected to move at a fraction of the local chord advection speed. The

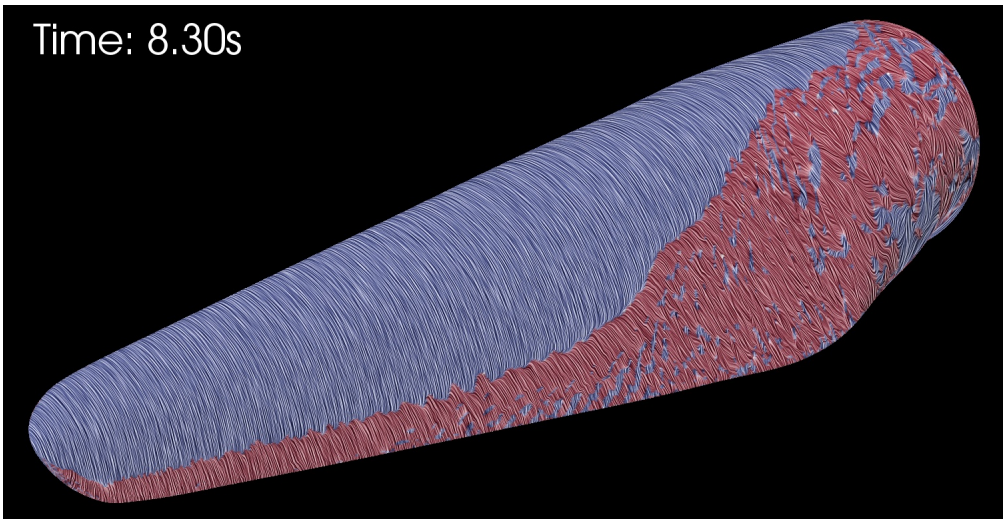

Figure 33: Surface separation streamlines at an instance in time in *SRBIA-58M*. The red regions indicate the separated region

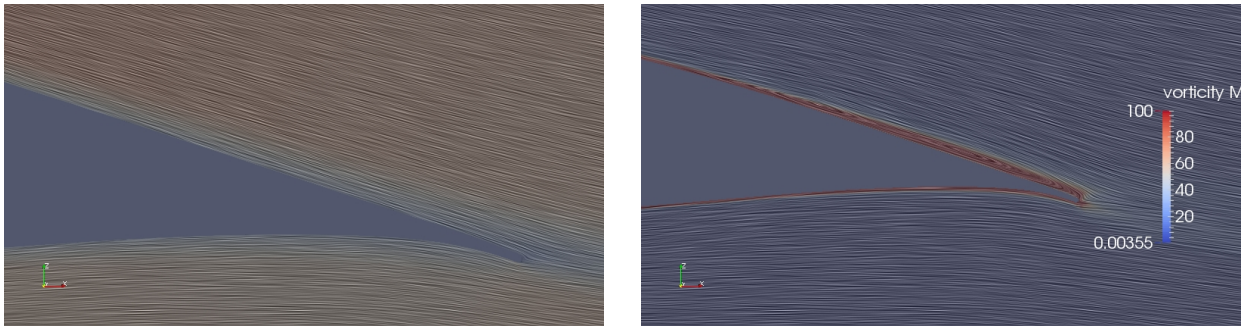

(a): Uniform inflow (b): ABL

Figure 34: Comparison of flow streamlines near the trailing edge of an airfoil in uniform inflow and in an ABL.

30 different radial stations on the blade used for this analysis are separated by a distance of 2m each. If the separation location were moving at half the local chord speed, then the time taken for the separation location to reach an adjacent radial section would be $\Delta t = 2.0c/U_c$, where c is the chord and U_c is the local chord advection speed. If there does exist a spanwise movement of the separation location in SRBIA, then the correlation coefficient must increase when a time delay is introduced between adjacent sections corresponding to the speed of the separation location. Since the, yet hypothetical, advection speed of the separation location is unknown, a time-delay correlation coefficient is computed for different possible speeds from 5% - 500% of the local chordwise advection speed. These results are also shown in Figure 36. Compared to the zero time delay case, the correlation coefficient seems to reduce for all possible time delays, indicating that there is no significant movement of the separation location in SRBIA. The correlation between adjacent separation points without any time delay is likely due to the angle of attack changing consistently between the two locations. The lack of spanwise movement of the boundary layer is attributed to the location of the wind turbine blade in a low speed streak as explained in Section III.B. The angle of attack on the blade is severely reduced in the low-speed streak and this prevents many airfoil stations from operating at a higher point in their respective $C_l - \alpha$ curves. To truly test the existence of spanwise motion of the separation location, *SRBIA* would need to be analyzed over a longer duration.

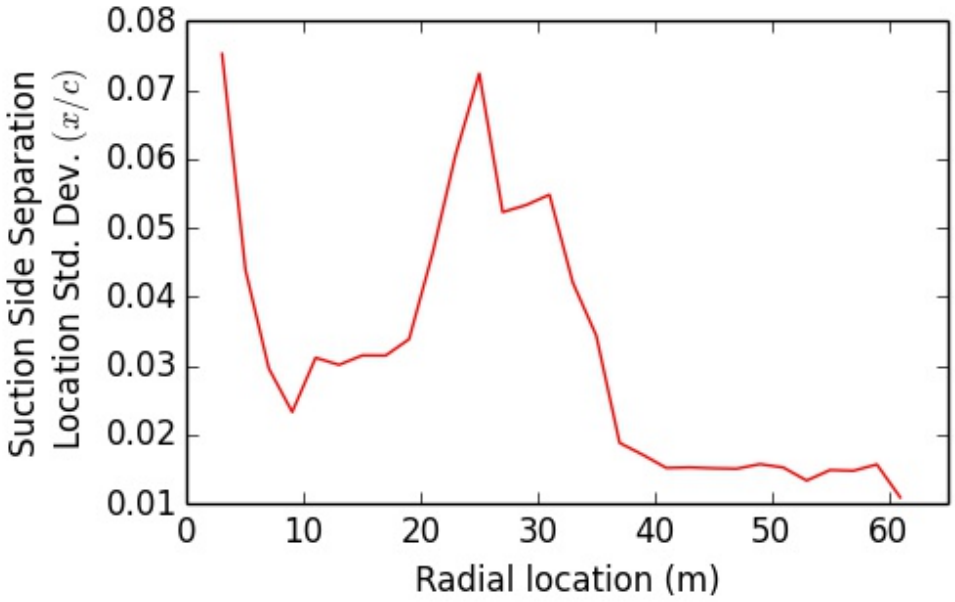

Figure 35: Standard deviation of separation location on the suction side in *SRBIA* simulation.

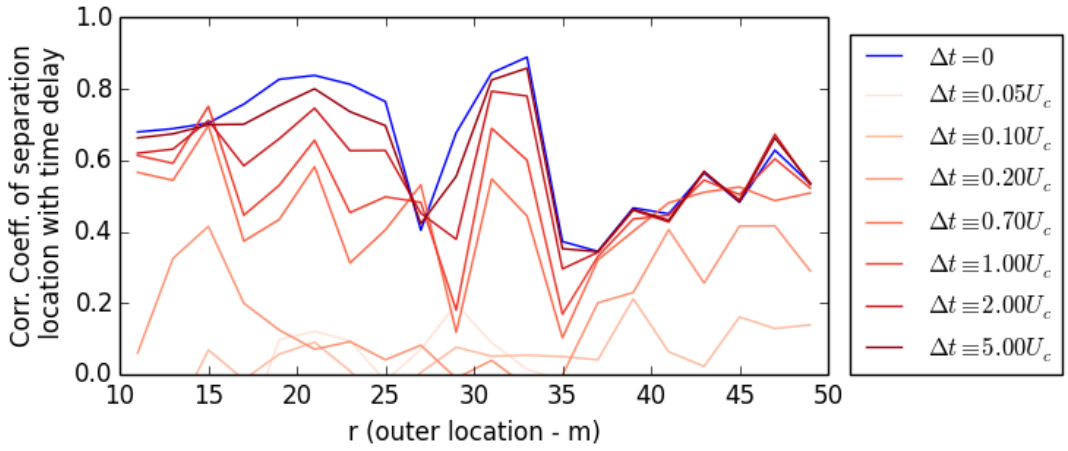

Figure 36: Correlation coefficient between adjacent sections with increasing time-delay.

IV. Summary and Conclusions

The interaction of atmospheric turbulence with unsteady wind turbine loads was analyzed through the development of the Blade Aerodynamics and Atmospheric Turbulence modules of the Cyber Wind Facility at Penn State. This interaction between the different turbulence dynamical systems is realized through a two-stage, one-way coupled process. A key element in the development of these modules was the integration of disparate range of scales from the large eddy scales in the atmosphere to the viscous layer of the blade boundary layer. Large Eddy Simulation was used to simulate a realistic day-time atmosphere over a flat land with surface roughness that is representative of the conditions in wind farms in the mid-west (for e.g. Texas, Iowa). The data from this simulation are used as inflow conditions to a different simulation to capture the effect of the atmospheric turbulence on unsteady wind turbine loads.

The characteristics of day-time atmospheric turbulence relevant to wind turbines was first analyzed placing hypothetical NREL 5MW turbines in the flow field generated by LES of ABL. The time scales of the energy-containing eddies in ABL as experienced by the wind turbines was found to be $\sim O$(multiple rotation time scales).

The knowledge of these time scales could be potentially used to tweak upcoming LIDAR based feed-forward control systems of wind turbines to increase power capture and improve their reliability.

We designed a computational framework to accurately propagate the turbulence structures in the ABL using a finite volume algorithm. A new hybrid URANS-LES framework was developed using a combination of grid design and blending of different turbulence models to compute the spatio-temporal oscillations on the wind turbine in a day-time atmospheric boundary layer. This computational framework was used to simulate a single rotating blade of the NREL 5MW turbine in the atmosphere using blade boundary layer resolved CFD simulations (*SRBIA*). The large fluctuations in the Angle of Attack observed on a wind turbine using previous analyses motivated the design of two grids for the *SRBIA* simulations to capture the expected three dimensional transient separation on the blade. *SRBIA-58M* and *SRBIA-9M* confirm that atmospheric turbulence causes most of the fluctuations in the loads on a wind turbine through changes in the angle of attack on individual blade sections. However, they find no significant three dimensional transient separation or spanwise flow on the blade. This is attributed to the low angles of attack created by the pitch setting corresponding to a wind speed of $14m/s$ while the average wind speed in the simulation was $11.53m/s$. While the 2D boundary layer separation on the blade does cause sectional load fluctuations at frequencies much greater than the blade rotation frequency, they are found to contain significantly less energy than those caused by fluctuations in the angle of attack. Hence, the outer parts of the blade are found to contribute the most to both the average and the fluctuations in the loads.

The integration of all the analyses performed in this work shows that wind turbines respond to atmpospheric turbulence at three different time scales with respect to the blade rotation time scale (t_{BR}): $t \gg t_{BR}$, $t \sim t_{BR}$ and $t < t_{BR}$. The dominant cause of the fluctuations is different at these three time scales. The energy-containing eddies in the ABL cause the fluctuations at the $t \gg t_{BR}$ time scale as the low-speed and high-speed streak eddies sweep past the turbine. A combination of shear and the rotation of the turbine through the ABL creates the fluctuations around the blade rotation frequency, while the latter is primarily responsible for the fluctuations at the $t < t_{BR}$ time scale. While the cause of the fluctuations may be different at different time scales, the resultant fluctuations in the angle of attack on the blade sections is the primary mechanism through which the fluctuations in the atmospheric turbulence are converted into load fluctuations on the turbine. The fluctuations in the angle of attack at an individual blade section are caused by the corresponding wind vector changes relative to the local chord of a rotating blade that are associated with the atmospheric turbulence structure. The fluctuations in angle of attack at a blade section create the load fluctuations through corresponding changes in flow separation around that section. The stability state of the atmosphere controls the turbulence structure in the surface layer and thus the changes in the wind vector direction experienced by a turbine.

The *SRBIA* simulations suggest that tools based on "table lookups" like FAST[1] and Actuator Line Method,[2] but appropriately modified using data from high-fidelity simulations such as in this work, have the potential to capture the major fluctuation events in integrated loads due to atmospheric turbulence eddies. This would need to be verified with longer simulations of SRBIA at different stability states and more eddy passages of different eddy types. The results of such a study could have a major impact on the choice of simulation tools for wind turbines in a realistic atmosphere.

Acknowledgments

We are grateful for support for this research by the National Science Foundation Sustainability Program under grant CBET 0933647, the Department of Energy Offshore wind program and the Innovation Grant program of the College of Engineering at Penn State. We also thank the E&F program from Penn State Applied Research Laboratory for funding support. This research was supported in part by the National Science Foundation through XSEDE resources provided by National Institute for Computational Sciences, Tennessee, Pittsburgh Computing Center and the Texas Advanced Computing Center under grant number TG-ATM110007. We are grateful to Drs. Jason Jonkman, Scott Schreck and Patrick Moriarty at the National Renewable Energy Laboratory for their help in tracking down the airfoil coordinates to the NREL 5MW wind turbine blade. We thank Dr. Nando Timmer at Delft University of Technology very much for providing us the coordinates to all DU airfoil sections, including the two previously proprietary sections.

References

[1]Jonkman, J., Butterfield, S., Musial, W., and Scott, G., "Definition of a 5-MW Reference Wind Turbine for Offshore System Development ," Tech. Rep. NREL/TP-500-38060, National Renewable Energy Laboratory, Feb. 2009.

[2]Churchfield, M. J., Lee, S., Moriarty, P., Martinez, L. A., Leonardi, S., Vijayakumar, G., and Brasseur, J. G., "Large-Eddy Simulations of Wind-Plant Aerodynamics," *50th Aerospace Sciences Meet and Exhibit*, 2012, AIAA 2012-0537.

[3]Manwell, J., McGowan, J. G., and Rogers, A. L., *Wind Energy Explained: Theory, Design and Application*, Wiley, 2nd ed., 2009.

[4]Robinson, S. K., "Coherent Motions in the Turbulent Boundary Layer," *Annual Review of Fluid Mechanics*, Vol. 23, No. 1, 1991, pp. 601–639.

[5]"Wind turbines - Part I: Design Requirements," Tech. Rep. ICE/61400-1, International Electrotechnical Commission, 2005.

[6]Wharton, S. and Lundquist, J. K., "Assessing Atmospheric Stability and its impacts on rotor-disk Wind Characteristics at an Onshore Wind farm," *Wind Energy*, 2011.

[7]Kelly, N. D. and Jonkman, B., "Overview of the TurbSim Stochastic Inflow Turbulence Simulator," *NREL/TP-500-41137*, April 2007.

[8]Lund, T. S., Wu, X., and Squires, K. D., "Generation of Turbulent Inflow Data for Spatially-Developing Boundary Layer Simulations," *Journal of Computational Physics*, Vol. 140, No. 2, 1998, pp. 233 – 258.

[9]Mann, J., "Wind field simulation," *Probabilistic Engineering Mechanics*, Vol. 13, No. 4, 1998, pp. 269 – 282.

[10]Spille-Kohoff, A. and Kaltenbach, H., "Generation of turbulent inflow data with a prescribed shear-stress profile," Tech. rep., DTIC Document, 2001.

[11]Sim, C., Manuel, L., and Basu, S., "A Comparison of Wind Turbine Load Statistics for Inflow Turbulence Fields based on Conventional Spectral Methods versus Large Eddy Simulation," *48th AIAA Aerospace Sciences Meeting Including the New Horizons Forum and Aerospace Exposition*, 2010, AIAA-2010-829.

[12]Auerswald, T., Weinreis, C., Bange, J., Raasch, S., and Radespiel, R., "Comparison Of High Resolution Large-Eddy Simulations And Synthetic Turbulent Wind Fields," *48th AIAA Aerospace Sciences Meeting Including the New Horizons Forum and Aerospace Exposition*, 2010, AIAA 2010-1253.

[13]Lavely, A. W., Vijayakumar, G., Kinzel, M. P., Brasseur, J. G., and Paterson, E. G., "Comparing Unsteady Loadings on Wind Turbines Using TurbSim and LES Flow Fields," *Aerospace Sciences Meetings*, American Institute of Aeronautics and Astronautics, Jan. 2012.

[14]Snel, H., "Review of Aerodynamics for Wind Turbines," *Wind Energy*, Vol. 6, No. 3, 2003, pp. 203–211.

[15]Snel, H., "Review of the present status of rotor aerodynamics," *Wind Energy*, Vol. 1, No. S1, April 1998, pp. 46–69.

[16]Hansen, M. O. L., Sørensen, J., Voutsinas, S., Sørensen, N. N., and Madsen, H. A., "State of the art in wind turbine aerodynamics and aeroelasticity," *Progress in Aerospace Sciences*, Vol. 42, No. 4, 2006, pp. 285 – 330.

[17]Lavely, A. W., Vijayakumar, G., Brasseur, J. G., Paterson, E. G., and Kinzel, M. P., "Inherent Variability in Short-time Wind Turbine Statistics from Turbulence Structure in the Atmospheric Surface Layer," Vol. 56, Presented at the 64th Annual Meeting of the APS Division of Fluid Dynamics, Baltimore, MD, Nov 2011.

[18]Leishman, J. G., "Challenges in modelling the unsteady aerodynamics of wind turbines," *Wind Energy*, Vol. 5, No. 2-3, 2002, pp. 85–132.

[19]Sullivan, P. P. and Patton, E. G., "A highly parallel algorithm for turbulence simulations in planetary boundary layers: Results with meshes up to 1024 cubed," *18th Conference on Boundary Layer and Turbulence*, 2008.

[20]Moeng, C.-H., "A Large-Eddy-Simulation Model for the Study of Planetary Boundary-Layer Turbulence," *Journal of the Atmospheric Sciences*, Vol. 41, No. 13, 1984, pp. 2052–2062.

[21]Brasseur, J. G. and Wei, T., " Designing large-eddy simulation of the turbulent boundary layer to capture law-of-the-wall scaling," *Physics of Fluids*, Vol. 22, No. 2, February 2010.

[22]Simms, D., Schreck, S., Hand, M., and Fingersh, L. J., "NREL Unsteady Aerodynamics Experiment in the NASA-Ames Wind Tunnel: A Comparison of Predictions to Measurements," Tech. Rep. NREL/TP-500-29494, National Renewable Energy Laboratory, June 2001.

[23]Le Pape, A. and Lecanu, J., "3D Navier-Stokes computations of a stall-regulated wind turbine," *Wind Energy*, Vol. 7, No. 4, 2004, pp. 309–324.

[24]Sørensen, N. N., Michelsen, J. A., and Schreck, S., "Navier-Stokes predictions of the NREL phase VI rotor in the NASA Ames 80 ft x 120 ft wind tunnel," *Wind Energy*, Vol. 5, No. 2-3, 2002, pp. 151–169.

[25]Lynch, C. and Smith, M., "Unstructured overset incompressible computational fluid dynamics for unsteady wind turbine simulations," *Wind Energy*, Vol. 16, No. 7, 2013, pp. 1033–1048.

[26]Potsdam, M. and Mavriplis, D., "Unstructured Mesh CFD Aerodynamic Analysis of the NREL Phase VI Rotor," *Aerospace Sciences Meetings*, American Institute of Aeronautics and Astronautics, Jan. 2009.

[27]Duque, E. P. N., Burklund, M. D., and Johnson, W., "Navier-Stokes and Comprehensive Analysis Performance Predictions of the NREL Phase VI Experiment," *Journal of Solar Energy Engineering*, Vol. 125, No. 4, 2003, pp. 457–467.

[28]Johansen, J., Sørensen, N. N., Michelsen, J. A., and Schreck, S., "Detached-eddy simulation of flow around the NREL Phase VI blade," *Wind Energy*, Vol. 5, No. 2-3, 2002, pp. 185–197.

[29]Sørensen, N. N. and Johansen, J., "UPWIND, aerodynamics and aero-elasticity, rotor aerodynamics in atmospheric shear flow," 2007.

[30]Bazilevs, Y., Hsu, M., Akkerman, I., Wright, S., Takizawa, K., Henicke, B., Spielman, T., and Tezduyar, T., "3D simulation of wind turbine rotors at full scale. Part I: geometry modeling and aerodynamics," *International Journal for Numerical Methods in Fluids*, Vol. 65, No. 1-3, 2011, pp. 207–235.

[31]Bazilevs, Y., Hsu, M.-C., Kiendl, J., Wuchner, R., and Bletzinger, K.-U., "3D simulation of wind turbine rotors at full scale. Part II: Fluid–structure interaction modeling with composite blades," *International Journal for Numerical Methods in Fluids*, Vol. 65, No. 1-3, 2011, pp. 236–253.

[32]Chow, R. and van Dam, C. P., "Computational investigations of blunt trailing-edge and twist modifications to the inboard region of the NREL-5MW rotor," *Wind Energy*, 2012.

[33]Chow, R. and van Dam, C. P., "Verification of computational simulations of the NREL-5MW rotor with a focus on inboard flow separation," *Wind Energy*, 2012.

[34]Zahle, F. and Sørensen, N. N., "Overset Grid Flow Simulation on a Modern Wind Turbine," *Guidance, Navigation, and Control and Co-located Conferences*, American Institute of Aeronautics and Astronautics, Aug. 2008.

[35]Vijayakumar, G., Brasseur, J. G., Lavely, A. W., Churchfield, M. J., Kinzel, M. P., Moriarty, P. J., and Paterson, E. G., "Considerations in coupling LES of the atmosphere to CFD around wind turbines," *50th AIAA Aerospace Sciences Meeting and Exhibit*, 2012, AIAA-2012-0817.

[36]"OpenFOAM: The Open Source CFD Toolbox - User Guide," Tech. rep., OpenFOAM foundation, 2011.

[37]Vijayakumar, G., Lavely, A. W., Jayaraman, B., Craven, B., and Brasseur, J. G., "Blade Boundary Layer Response to Atmospheric Boundary Layer Turbulence on a NREL 5MW Wind Turbine Blade with Hybrid URANS-LES," *52nd Aerospace Sciences Meet and Exhibit*, Jan. 2014, AIAA-2014-0867.

[38]Spalart, P. R., Strelets, M. K., and Travin, A., "Expectations in the Wall Region of a Large-Eddy Simulation," *Quality and Reliability of Large-Eddy Simulations*, edited by J. Meyers, B. J. Geurts, and P. Sagaut, Vol. 12 of *ERCOFTAC Series*, Springer Netherlands, 2008, pp. 181–191.

[39]Spalart, P. R., "Detached-Eddy Simulation," *Annual Review of Fluid Mechanics*, Vol. 41, No. 1, 2009, pp. 181–202.

[40]Piomelli, U. and Balaras, E., "Wall-Layer Models for Large Eddy Simulations," *Annual Review of Fluid Mechanics*, Vol. 34, No. 1, 2002, pp. 349–374.

[41]Spalart, P. R., Jou, W.-H., Strelets, M., and Allmaras, S. R., "Comments on the feasibility of LES for wings, and on a hybrid RANS/LES approach," *Advances in DNS/LES ed. C. Liu, Z. Liu*, 1997.

[42]Spalart, P. R., "A One-Equation Turbulence Model for Aerodynamic Flows," *La Recherche Aerospatiale*, Vol. 1, 1994, pp. 5–21.

[43]Travin, A., Shur, M., Strelets, M., and Spalart, P. R., "Physical and Numerical Upgrades in the Detached-Eddy Simulation of Complex Turbulent Flows," *Advances in LES of Complex Flows*, edited by R. Friedrich and W. Rodi, Vol. 65 of *Fluid Mechanics and Its Applications*, Springer Netherlands, 2004, pp. 239–254.

[44]Sørensen, N. N. and Schreck, S., "Computation of the National Renewable Energy Laboratory Phase-VI rotor in pitch motion during standstill," *Wind Energy*, 2011.

[45]Stone, C., Lynch, C., and Smith, M., "Hybrid RANS/LES Simulations of a Horizontal Axis Wind Turbine," *48th AIAA Aerospace Sciences Meeting Including the New Horizons Forum and Aerospace Exposition*, 2010.

[46]Mockett, C., *A Comprehensive Study of Detached-Eddy Simulation*, Ph.D. thesis, Technical University of Berlin, 2009.

[47]Frahlich, J. and von Terzi, D., "Hybrid LES/RANS methods for the simulation of turbulent flows," *Progress in Aerospace Sciences*, Vol. 44, No. 5, 2008, pp. 349 – 377.

[48]Shur, M. L., Spalart, P. R., Strelets, M. K., and Travin, A. K., "A hybrid RANS-LES approach with delayed-DES and wall-modelled LES capabilities," *International Journal of Heat and Fluid Flow*, Vol. 29, No. 6, 2008, pp. 1638 – 1649.

[49]Spalart, P. R., Deck, S., Shur, M., Squires, K., Strelets, M., and Travin, A., "A New Version of Detached-eddy Simulation, Resistant to Ambiguous Grid Densities," *Theoretical and Computational Fluid Dynamics*, Vol. 20, 2006, pp. 181–195.

[50]Strelets, M., "Detached Eddy Simulation of Massively Separated Flows," *39th AIAA Aerospace Sciences Meeting and Exhibit*, January 2001, AIAA 2001-0879.

[51]Spalart, P. R., "Young-person's guide to detached-eddy simulation grids," Tech. Rep. NASA/CR-2001-211032, National Aeronautics and Space Administration, Langley Research Center, July 2001.

[52]Nikitin, N. V., Nicoud, F., Wasistho, B., Squires, K. D., and Spalart, P. R., "An approach to wall modeling in large-eddy simulations," *Physics of Fluids*, Vol. 12, No. 7, July 2000, pp. 1629–1632.

[53]Menter, F., Kuntz, M., and Bende, R., "A scale-adaptive simulation model for turbulent flow prediction," *AIAA Paper 2003-0767*, 2003.

[54]Egorov, Y. and Menter, F., "Development and Application of SST-SAS Turbulence Model in the DESIDER Project," *Advances in Hybrid RANS-LES Modelling*, edited by S.-H. Peng and W. Haase, Vol. 97 of *Notes on Numerical Fluid Mechanics and Multidisciplinary Design*, Springer Berlin / Heidelberg, 2008, pp. 261–270.

[55]Menter, F. and Egorov, Y., "The Scale-Adaptive Simulation Method for Unsteady Turbulent Flow Predictions. Part 1: Theory and Model Description," *Flow, Turbulence and Combustion*, Vol. 85, 2010, pp. 113–138.

[56]Egorov, Y., Menter, F., Lechner, R., and Cokljat, D., "The Scale-Adaptive Simulation Method for Unsteady Turbulent Flow Predictions. Part 2: Application to Complex Flows," *Flow, Turbulence and Combustion*, Vol. 85, 2010, pp. 139–165.

[57]Pope, S. B., *Turbulent Flows*, Cambridge University Press, 2005.

[58]Chaviaropoulos, P. and Hansen, M., "Investigating Three-Dimensional and Rotational Effects on Wind Turbine Blades by Means of a Quasi-3D Navier-Stokes Solver," *Journal of Fluids Engineering*, Vol. 122, No. June 2000, 2000, pp. 330–336.

[59]Guntur, S. and Sørensen, N. N., "Evaluation of several methods of determining the angle of attack on wind turbine blades," *Science of Making Torque from Wind*, 2012.

[60]Hand, M., Simms, D., Fingersh, L. J., Jager, D., Schreck, S., Cotrell, J., and Larwood, S., "Unsteady aerodynamics experiment phases VI: wind tunnel test configurations and available data campaigns." , No. NREL/TP-500-29955, 2001.

[61]Medina, P., Singh, M., Johansen, J., Rivera Jove, A., Machefaux, E., Fingersh, L., and Schreck, S., "Aerodynamic and Performance Measurements on a SWT-2.3-101 Wind Turbine," Tech. Rep. NREL/CP-5000-51649, National Renewable Energy Laboratory, 2011.

[62]Hansen, M. O. L., *Aerodynamics of Wind Turbines*, Earthscan, 2nd ed., 2008.

[63]Leishman, G. J., *Principles of Helicopter Aerodynamics*, Cambridge Aerospace Series, 2006.

[64]Ericsson, L. and Reding, J., "Fluid mechanics of dynamic stall part I. Unsteady flow concepts ," *Journal of Fluids and Structures*, Vol. 2, No. 1, 1988, pp. 1 – 33.

[65]Delery, J. M., "Robert Legendre and Henri Werle: Toward the Elucidation of Three-DimensionalSeparation," *Annual Review of Fluid Mechanics*, Vol. 33, No. 1, 2001, pp. 129–154.

[66]Schreck, S., "Shedding Kinematics and Underlying Flow Field Physics on Rotating Turbine Blades," *Aerospace Sciences Meetings*, American Institute of Aeronautics and Astronautics, Jan. 2008, pp. –.